

On trajectory design from motion primitives for near time-optimal transitions for systems with oscillating internal dynamics

1st Thomas Auer
IACE - UMIT TIROL
Hall in Tirol, Austria
thomas.auer@umit-tirol.at

2nd Frank Woittennek
IACE - UMIT TIROL
Hall in Tirol, Austria
frank.woittennek@umit-tirol.at

Abstract—An efficient approach to compute near time-optimal trajectories for linear kinematic systems with oscillatory internal dynamics is presented. Thereby, kinematic constraints with respect to velocity, acceleration and jerk are taken into account. The trajectories are composed of several motion primitives, the most crucial of which is termed jerk segment. Within this contribution, the focus is put on the composition of the overall trajectories, assuming the required motion primitives to be readily available. Since the scheme considered is not time-optimal, even decreasing particular constraints can reduce the overall transition time, which is analysed in detail. This observation implies that replanning of the underlying jerk segments is required as an integral part of the motion planning scheme, further insight into which has been analysed in a complementary contribution. Although the proposed scheme is not time-optimal, it allows for significantly shorter transition times than established methods, such as zero-vibration shaping, while requiring significantly lower computational power than a fully time-optimal scheme.

Index Terms—Motion and Path Planning, Optimization and Optimal Control, Motion Control, Semiconductor Manufacturing

I. INTRODUCTION

Pick-and-place processes in the electrical industry demand accuracy and speed. Trends in the electronics industry point to miniaturisation and further integration of circuits from year to year [53], [50], [32], [29]. High accuracy is required for part placement to ensure electrical connections work as intended. In order to decrease cost, short transitions are desirable. Forces due to motion acting on the machine frame in combination with finite stiffness lead to oscillation and inaccuracy in component placement, as well as increased machine wear [26], [55]. The oscillation amplitudes of the machine frame can be bigger, than the allowed accuracy requirements, which are fractions of μm 's [50], [32], [29]. Specifically planned motion profiles, also called trajectories, are used to achieve rest-to-rest transitions for the system.

This work has been submitted to the IEEE for possible publication. Copyright may be transferred without notice, after which this version may no longer be accessible.

A. Previous research in this topic

The so called S-Curve [19] is the fastest time optimal trajectory, that is limited in jerk, acceleration and velocity for rest-to-rest transitions of ideally stiff systems. Since production machines exhibit flexibility originating from the finite stiffness of the machine frame, it is usually not feasible to use the S-Curve directly, since it leads to oscillation. A method to plan rest-to-rest trajectories for systems exhibiting flexibility is the application of shaping techniques to those trajectories. This is commonly referred to as trajectory shaping. A common shaper, that is used for this purpose is the zero-vibration (ZV)-shaper [25], [23]. A key advantage of trajectory shapers lies in its ease of implementation and the robustness w.r.t. to parameter uncertainty [36]. The sensitivity to parameter uncertainty of the ZV-shaper can be further reduced by increasing the system damping [23]. Further and more substantial improvements can be achieved by utilizing ZVD-shapers [52], [31], [30] or EI-shapers [6], [18], [24]. A very detailed overview concerning the shaping methods can be found in [20]. Decreasing the sensitivity to parameter uncertainty has been studied extensively, because it is an important topic. However, if the parameters of the system are known with a certain accuracy, methods offering shorter transition times can be of greater interest. A method to decrease transition times, when using trajectory shapers is to employ negative-impulse shapers [27]. However, even if the original trajectory does not violate any kinematic constraints, due to the nature of negative-impulse shapers, violations of kinematic constraints can occur for the shaped trajectory. While there are strategies to avoid violation of kinematic constraints [1] and negative-impulse shapers allow for faster transitions, they are limiting the shape of the underlying trajectory and might still lack time-optimality in order to avoid violation of the kinematic constraints. Methods to adjust the underlying S-Curve trajectories in order to remove as much oscillation as possible have been studied in [7], [13], [21]. By adjusting the maximal jerk and the duration, considerable amounts of oscillation can be removed without utilizing trajectory shapers. The general idea has also been extended (FIR-methods) and developed for full

trajectories [8], [2], [10], [47], [45], [40], leading to a potential reduction of transition time at the expense of sensitivity to parameter uncertainty. A drawback of these approaches is, that the damping of the system cannot be taken into account, even if it is known. This leads to residual oscillation, even for the nominal model (no parameter uncertainty). It is possible to account for system damping according to [13]. However, this has not been applied to the expanded full trajectories.

Employing feedback control concepts is a further possibility to improve the oscillation behaviour [11], [39], [15], [37]. This allows to use fast shapers or trajectories planned without shapers and the insensitivity to parameter uncertainty can be ensured by the active control concept [14]. Approaches with feedback still benefit from fast trajectories that offer rest-to-rest transitions for the nominal model [43]. In this case, the controller reduces the oscillation at the end of a transition. A disadvantage is, that additional measurement equipment might be required. Using trajectories planned to achieve oscillation free rest-to-rest transitions is still beneficial. Trajectories planned with optimal-control approaches guarantee the fastest transitions while respecting the kinematic constraints. Different planning methods including two optimal-control concepts were compared in [4]. Calculation through optimization of truly time-optimal trajectories can cause issues due to the discontinuous nature of the input signals required [33]. Implementation of the required numeric algorithms on programmable logic controllers (PLC) can be especially problematic due their limited computing power. Another issue that prevents such approaches from being used in actual pick-and-place machines consists in the lack of guarantees concerning the convergence of the underlying algorithms. This is particularly problematic in cases where it is not possible to pre-calculate and store trajectories, for example, when system parameters are constantly updated by measurements. A method to plan the motion out of trajectory segments, where each segment has to satisfy a number of constraints has been proposed in [35]. This method offers a time-advantage over a ZV-shaped trajectory at the expense of more complicated calculation, however the calculation effort required can be prohibitive, when it comes to using it on industrial machinery.

B. Contribution of this paper to the field

This publication introduces the trajectory planning method called OCP-J. Here, the full trajectories are assembled from individual motion primitives (which are themselves computed in a time-optimal manner, as explained in [42]). Crucially, in order to ensure minimal transition times of the complete trajectories, the proposed algorithm allows overlapping of individual motion primitives while avoiding a violation of the kinematic constraints. Moreover, this publication shows that lowering the acceleration limit for the proposed approach can lead to faster overall rest-to-rest transitions. It allows for faster transitions than the existing ZV-shaper and offers better behaviour w.r.t. sensitivity to parameter uncertainty than FIR-methods. The analyses presented compare the time advantages with other trajectory planning approaches and shows the sensitivity to

parameter uncertainty. An extensive measurement study performed on a laboratory system (with all of the trajectories calculated on the laboratory system's PLC) demonstrates and validates the OCP-J approach and highlights its performance characteristics. Furthermore, because the calculation is not based on an iterative numerical optimization, but on direct calculation, the computation time is known, constant and sufficiently small to allow trajectories to be calculated as they are needed. This allows the system parameters to be continuously updated to take parameter drift into account.

C. Organisation of paper

The mathematical model, the parameters and the most important mathematical background are presented in Section II. Then the calculation of the full trajectory with the three different cases is explained in Section III. The formulation of an overlying optimization problem to ensure minimum transition times with the OCP-J approach is described in Section IV and the algorithms required are also summarised there. This section shows why the quick calculation of the jerk segments may be an advantage in some cases (cf. [42] for the algorithm). A comparison with other existing approaches (commonly used in the field and newly developed) in terms of transition time and parameter sensitivity is given in Section V. This comparison is extended to different parameter sets for a more detailed analysis. Eventually, measurement results from a laboratory system are used to validate the approach in Section VI. The results are then discussed in Section VII and points for relevant follow-up research are provided in Section VIII.

II. PRELIMINARIES

This section presents a mathematical model of a system to which the presented trajectory planning method can be applied. As the equations used for calculation in this publication and in [42] (calculation of motion primitives) show, the trajectory planning approach is solely influenced by the kinematic constraints of the actuator and the system's oscillatory behaviour. The kinematic constraints are the maximum velocity v_{lim} , acceleration a_{lim} and jerk j_{lim} , while the systems behaviour is characterised by the eigenfrequency ω_d and damping factor δ , which is allowed to be zero. The laboratory system used to validate the approach via measurements corresponds to the model presented. The use of this model as a basis allows for better presentation, while also maintaining the possibility of its application to other systems.

A. Mathematical model

A pick-and-place machine exhibiting flexibility could be modelled using a continuum mechanic description, if every effect of the oscillation should be captured in detail. However, since the essential oscillation of the machine frame can be captured by the first mode, a simplified system description with a lumped model has been chosen. This model consists of two masses, a spring and a viscous damping element and is shown schematically in Figure 1. While this is a rather

simple system, it is sufficient in modelling the motion and the focus of the contribution can be put on the effective method of calculation of the trajectory. The spring k represents the stiffness of the machine frame and the viscous damping element d the natural damping of the machine frame. The masses are the mass of the baseframe m_b and the mass of the slider m_s . In an actual production machine this slider would mount a gripper for component handling and it is commonly referred to as endeffector. The equations governing the motion

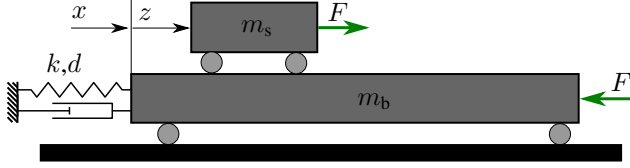


Fig. 1: Symbolic representation of one axis of the pick-and-place machine.

of the system [4, cf.] can be derived via momentum balance and are given by

$$m_b \ddot{x}(t) + d \dot{x}(t) + k x(t) = -F(t), \quad (1a)$$

$$m_s (\ddot{x}(t) + \ddot{z}(t)) = F(t), \quad (1b)$$

whereas any effects arising from friction are included in the force $F(t)$. Using a position controller for the slider position $z(t)$ on the actual production machines removes the influence of those forces by basically using $\ddot{z}(t)$ as input. The parameters used for the simulation studies in this contribution are listed in Table I. The kinematic constraints listed in Table II correspond

TABLE I: Parameters and resulting eigenfrequencies

$m_s = 25 \text{ kg}$	$m_b = 500 \text{ kg}$	$k = 15 \cdot 10^6 \text{ N/m}$	$d = 5 \cdot 10^3 \text{ kg/s}$
$f_0 = 26.9 \text{ Hz}$		$f_d = 26.8914 \text{ Hz}$	

to an exemplary production machine. All limits are imposed by the physical limits of the drives while, additionally, the jerk constraint has an influence on wear and tracking accuracy [17], [46], [22], [12], [55]. The kinematic constraints result from values provided by an industrial partner. It is advantageous

TABLE II: Kinematic constraints of slider.

$ \dot{z}(t) \leq v_{\text{lim}}$	$ \ddot{z}(t) \leq a_{\text{lim}}$	$ z^{(3)}(t) \leq j_{\text{lim}}$
$v_{\text{lim}} = 1.5 \text{ m/s}$	$a_{\text{lim}} = 20 \text{ m/s}^2$	$j_{\text{lim}} = 800 \text{ m/s}^3$

to use a dynamic extension with $z^{(3)}(t)$ as input for the calculations required later on. Adding (1a) and (1b) together to remove $F(t)$ and using $m_g = m_s + m_b$ leads to the state-space representation

$$\dot{\mathbf{x}} = \begin{bmatrix} 0 & 1 & 0 & 0 & 0 \\ -k^* & -d^* & 0 & 0 & -m^* \\ 0 & 0 & 0 & 1 & 0 \\ 0 & 0 & 0 & 0 & 1 \\ 0 & 0 & 0 & 0 & 0 \end{bmatrix} \cdot \begin{bmatrix} x \\ \dot{x} \\ z \\ \dot{z} \\ \ddot{z} \end{bmatrix} + \begin{bmatrix} 0 \\ 0 \\ 0 \\ 0 \\ 1 \end{bmatrix} z^{(3)} \quad (2)$$

$k^* = k/m_g \quad d^* = d/m_g \quad m^* = m_s/m_g$

with the state \mathbf{x} and input u given by

$$\mathbf{x} = [x, \dot{x}, z, \dot{z}, \ddot{z}]^T, \quad u = z^{(3)}. \quad (3)$$

If z is understood as the output of the system it can be readily observed that the system possesses relative degree 3 and is given in Byrnes-Isidori form. The internal dynamics, which obviously is not observable over this output corresponds to a damped harmonic oscillator with undamped eigenfrequency $\omega_0 = \sqrt{k^*}$ and damping ratio $\frac{d^*}{2\omega_0}$, which is excited by the slider acceleration \ddot{z} .

B. Solution of the slider dynamics

Twice continuously differentiable trajectories $t \mapsto z(t)$ are considered, which are piecewise constant in the input $u(t) = z^{(3)}(t)$. As a consequence, the jerk $z^{(3)}(t)$ is a sum of n steps of amplitudes a_1, \dots, a_n occurring at $t_1 < \dots < t_n$:

$$z^{(3)}(t) = \sum_{i=1}^n a_i H(t - t_i). \quad (4)$$

Therein, $H(\cdot)$ represents the Heaviside step function. The terminal time of the trajectory motion is denoted by $t_{f,t}$. Integration of (4) leads to

$$\ddot{z}(t) = \ddot{z}(0) + \sum_{i=1}^n a_i H(t - t_i) \cdot (t - t_i), \quad (5a)$$

$$\dot{z}(t) = \dot{z}(0) + \ddot{z}(0) t + \frac{1}{2} \sum_{i=1}^n a_i H(t - t_i) \cdot (t - t_i)^2, \quad (5b)$$

$$z(t) = z(0) + \dot{z}(0) t + \ddot{z}(0) \frac{t^2}{2} + \frac{1}{6} \sum_{i=1}^n a_i H(t - t_i) \cdot (t - t_i)^3. \quad (5c)$$

As the considered trajectories should correspond to rest-to-rest transitions of the slider, they must satisfy¹

$$z^{(3)}(0) = 0, \quad \ddot{z}(0) = 0, \quad \dot{z}(0) = 0, \quad (6a)$$

$$z^{(3)}(t_{f,t}) = 0, \quad \ddot{z}(t_{f,t}) = 0, \quad \dot{z}(t_{f,t}) = 0. \quad (6b)$$

Evaluating the initial and final conditions (6) in view of (4) and (5) yields the following relations for the coefficients in (4):

$$\sum_{i=1}^n a_i = 0, \quad \sum_{i=1}^n a_i t_i = 0, \quad \sum_{i=1}^n a_i t_i^2 = 0.$$

An example for such a trajectory is the so-called S-Curve [19] which is also used as reference trajectory in ZV and ZVD-shaping as shown in Figure 2.

¹Formally, the condition $z^{(3)}(t_{f,t}) = 0$ is not really required in the formulation of the corresponding optimal control problem. However, it can always be satisfied by choosing $t_n = t_{f,t}$ with an appropriate choice of a_n , leaving $t \rightarrow z^{(i)}(t)$, $i = 0, 1, 2$ unchanged on $[0, t_{f,t}]$. In fact, it ensures $\ddot{z}(t) = \dot{z}(t) = 0$ not only at $t = t_{f,t}$ but for all $t \geq t_{f,t}$, i.e., the system remains in the desired equilibrium. Moreover, the formulation chosen essentially simplifies the algebraic computations.

C. Optimal control formulation

For a general time-invariant non-linear system with state-space description

$$\dot{\mathbf{x}} = \mathbf{f}(\mathbf{x}(t), \mathbf{u}(t)), \quad \mathbf{x}(t) \in \mathbb{R}^n, \mathbf{u}(t) \in \mathbb{R}^m \quad (7)$$

an optimal control problem aims to compute the minimum

$$\min_{\mathbf{x}, \mathbf{u}, t_{f,t}} J(\mathbf{x}, \mathbf{u}, t_{f,t}), \quad (8a)$$

of a cost functional

$$J(\cdot) = V(\mathbf{x}(t_{f,t}), t_{f,t}) + \int_0^{t_{f,t}} \ell(\mathbf{x}(t), \mathbf{u}(t), t) dt, \quad (8b)$$

involving the Lagrangian ℓ and the Mayer term V (cf. [51], [41] for details). Thereby, for $t \in [0, t_{f,t}]$ the variables \mathbf{x} and \mathbf{u} are constrained by the state-space equation (7) and

$$\mathbf{u}(t) \in \mathcal{U}, \quad \mathbf{x}(t) \in \mathcal{X}, \quad \mathbf{x}(0) \in \mathcal{X}_0, \quad \mathbf{x}(t_{f,t}) \in \mathcal{X}_f.$$

Start- and terminal-conditions of the state are taken into account by $\mathcal{X}_0 \subset \mathbb{R}^n$ and $\mathcal{X}_f \subset \mathbb{R}^n$ respectively. The state is constrained to the subset $\mathcal{X} \subset \mathbb{R}^n$ and the input to $\mathcal{U} \subset \mathbb{R}^m$.

The main objective of contribution consists in computing time-optimal trajectories or at least nearly time-optimal rest-to-rest trajectories for the system (2). The corresponding optimal control problem [3] is obtained by using the terminal time of the transition $t_{f,t}$ directly as cost

$$J(\cdot) = t_{f,t},$$

which corresponds to the choice $\ell(\mathbf{x}(t), \mathbf{u}(t), t) = 1$ and $V(\mathbf{x}(t_{f,t}), t_{f,t}) = 0$ in (8b). Moreover, (7) is replaced by (3), and the initial and terminal constraints are given by

$$\begin{aligned} \mathbf{x}(0) &= [0, 0, 0, 0, 0]^T, \\ \mathbf{x}(t_{f,t}) &= [0, 0, z_f, 0, 0]^T \end{aligned}$$

with $z_f = z(t_{f,t})$ being the target point for the transition $t_{f,t}$. As a consequence, the complete system including the internal dynamics is at rest at the end of the slider transition as long as u is chosen according to $u(t) = z^{(3)}(t) = 0$, $t \geq t_{f,t}$. The state variables concerning the slider motion $\dot{z}(t)$ and $\ddot{z}(t)$ as well as the input $z^{(3)}(t)$ are constrained according to the limits given in Table II. The trajectory presented in Figure 2 has been calculated using a full discretization approach [34], [38], [44], [49], [3] to solve this optimization problem. If the optimization problem is formulated for the entire transition and solved in one step, the method is called OCP-S in this contribution. An exemplary trajectory is shown in Figure 2 and it is compared to the S-Curve trajectory [19] and a trajectory calculated with a ZV-shaper [25]. The transition distance of 300 mm shown can be considered a large distance in the context of the pick-and-place machines considered. The S-Curve represents the fastest transition from a start-point to an end-point, while respecting the kinematic constraints from Table II. However, the excitation of the internal dynamics of the system leads to oscillation and as a result to a loss of accuracy. ZV-shaping is a common method to achieve rest-to-rest transitions. The two main drawbacks of OCP-S are the effort for computing the

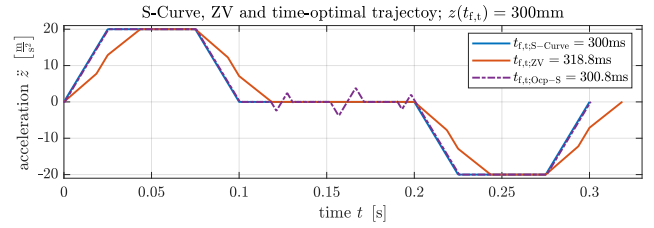


Fig. 2: Trajectories: S-Curve, ZV and OCP-S for a comparison of transition times for the motion distance $z(t_{f,t}) = 300$ mm.

trajectory (calculation time) and the sensitivity to parameter uncertainties [4]. For this reason [4] included a comparison to a method called OCP-J. In OCP-J, the trajectory for the full transition is assembled from preplanned motion primitives. A comparison to existing trajectory planning methods is shown in Section V (Figure 14 in Section V expands the comparison shown in Figure 2 to also include the OCP-J and FIR_{Imp} trajectory) and in greater detail also in [4]. This contribution explains the algorithms and mathematical background used for this second method (OCP-J) in detail and highlights the advantages.

III. METHOD EXPLAINED: OCP-J

This section provides an overview over OCP-J. Instead of solving an optimization problem for the whole trajectory like OCP-S, the OCP-J method assembles trajectories from motion primitives, some of them are the solution of smaller optimization problems. The proposed method is strongly inspired by the standard S-Curve (cf. [19]). However, in contrast to the latter, which constitutes the time-optimal trajectory when neglecting the internal dynamics in (2), OCP-J does not result in an exact solution of the optimal-control problem (8a). For fixed kinematic constraints and given plant parameters, the particular sequence of motion primitives depends on the terminal position z_f . Exemplary trajectories planned with this method are shown in Figure 3. The trajectory on the left represents

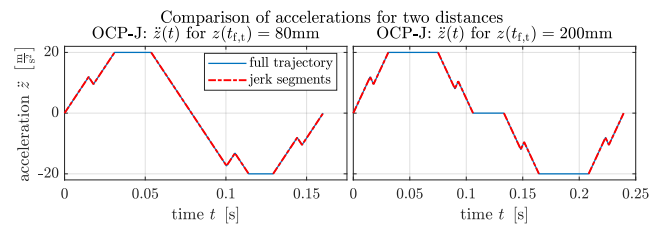


Fig. 3: Two OCP-J trajectories illustrating the method (picture taken from [4]).

a rather short transition distance, where only the maximum acceleration a_{lim} is reached, but not the maximum velocity v_{lim} . In contrast, the trajectory on the right corresponds to a larger distance, where both a_{lim} and v_{lim} are reached. In both trajectories the segments coloured in red are crucial. These motion primitives are called jerk segments in this paper and are designed such that the internal dynamics at the beginning

and at the end of these segments are at rest. A step-by-step explanation of how these are calculated using a direct method that does not rely on optimization can be found in [42]. This results in an optimization problem similar to the one introduced in the previous section. The initial conditions and terminal constraints at the free end time $t = t_f$ are given by

$$\ddot{x}(0) = -k^*x(0) - m^*\ddot{z}(0) = 0, \quad \dot{x}(0) = 0 \quad (10a)$$

$$\ddot{x}(t_f) = -k^*x(t_f) - m^*\ddot{z}(t_f) = 0, \quad \dot{x}(t_f) = 0. \quad (10b)$$

Moreover, within this contribution the following initial and terminal constraints for the acceleration segments are considered

$$\ddot{z}(t_f), \ddot{z}(0) \in \{-a_{\max}, 0, a_{\max}\}, \quad \ddot{z}(0) \neq \ddot{z}(t_f).$$

Moreover, the terminal velocity and terminal position are unconstrained while initial values $z(0)$ and $\dot{z}(0)$ may be specified. Above, the maximal acceleration a_{\max} does not necessarily coincide with² a_{\lim} .

By choosing the duration the slider moves at constant acceleration (resp. velocity) appropriately, the total transition distance can be adjusted (cf. Figure 3). Within this contribution several cases requiring different calculations for trajectory planning are considered. Their dependence on the final position z_f is illustrated in Figure 4 and characterized as follows:

- **Case 1:** A trajectory, where a_{\max} is reached, but v_{\lim} is not reached and there is only one jerk segment to get from a_{\max} to $-a_{\max}$.
- **Case 2:** A trajectory, where a_{\max} and v_{\lim} are reached.
- **Case 3:** A trajectory, where a_{\max} is reached and v_{\lim} is not reached. This case exists for distances too large for Case 1, but too small for Case 2. It is rare and only required for certain distances as shown in Figure 4. This special case is considered in Subsection III-D.

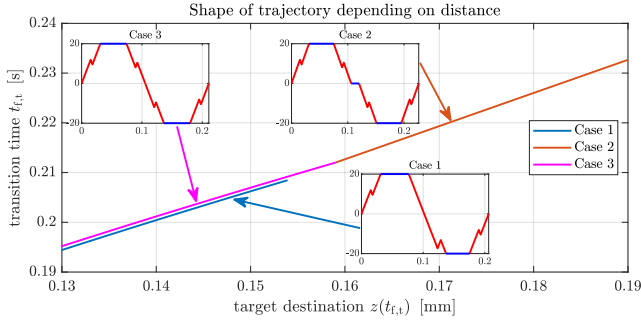


Fig. 4: Trajectories for multiple distances and regions associated with different cases.

A. Preprocessing of jerk segments

As Algorithm 1 describes, after calculating the jerk segments for the given a_{\max} , the velocity differences (v_{f1}, t_2, t_3)

²Note that, due to the particular construction of the trajectories it can be beneficial to choose $a_{\max} < a_{\lim}$ where a_{\lim} is the limit according to the specification. This is emphasized in Subsection III-E.

and some travel distances (s_{f1}, t_2, t_3) for the segments themselves have to be calculated. Those values are required when computing the full trajectories. The jerk segments and the corresponding parameters are highlighted in Figure 5 as a part of a particular trajectory. Although this trajectory corresponds to Case 1, the parameters computed also apply the remaining cases. The jerk $z^{(3)}(t)$ of the jerk segments is piece-wise constant, as depicted in Figure 3 and shown in [42]. As a consequence, it can be written in the form (4). Therefore, the corresponding velocity and the position result from (5). Following this procedure, the parameters s_{f1} and v_{f1} , associated with the first jerk segment, are given by

$$s_{f1} = z(t_{f1}), \quad v_{f1} = \dot{z}(t_{f1}),$$

where $t \mapsto z(t)$ and t_{f1} can be computed by minimizing t_{f1} subject to the given kinematic constraints and the system dynamics (2). The latter is complemented by the initial and final conditions, given by (10) and

$$z(0) = 0, \quad \dot{z}(0) = 0, \quad \ddot{z}(0) = 0, \quad \ddot{z}(t_{f1}) = a_{\max}.$$

Moreover, $s_{f2} = z(t_{f2})$, $v_{f2} = \dot{z}(t_{f2})$ are obtained in the same way for initial and terminal conditions

$$z(0) = 0, \quad \dot{z}(0) = 0, \quad \ddot{z}(0) = a_{\max}, \quad \ddot{z}(t_{f2}) = -a_{\max}.$$

Finally, t_{f3} , $s_{f3} = z(t_{f3})$, and $v_{f3} = -\dot{z}(t_{f3})$ follow from the boundary conditions

$$z(0) = 0, \quad \dot{z}(0) = 0, \quad \ddot{z}(0) = -a_{\max}, \quad \ddot{z}(t_{f3}) = 0.$$

B. Case 1

The general shape of the solution is shown in Figure 5. In order to reach the desired final position with the slider, the jerk segments have to be connected by segments with constant acceleration. In particular, acceleration $\ddot{z}(t)$ remains at a_{\max} during the intervals $[T_1, T_2]$ of duration t_1 and at $-a_{\max}$ during the interval $[T_3, T_4]$ of duration t_2 as shown in Figure 5. To compute the durations t_1 and t_2 , the precomputed

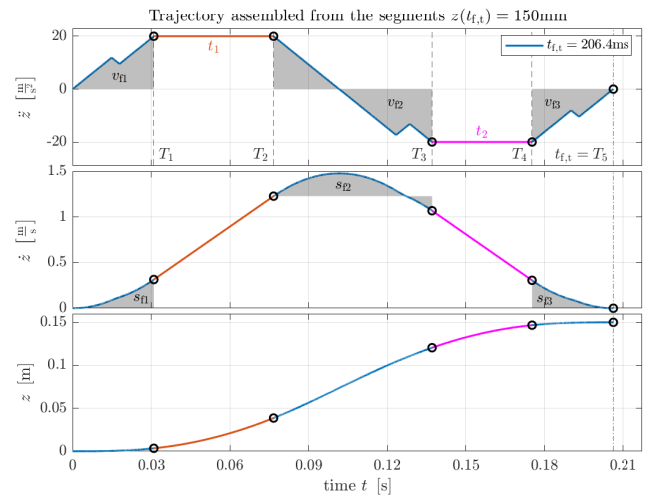


Fig. 5: OCP-J trajectory for Case 1.

values $s_{f1, f2, f3}$ and $v_{f1, f2, f3}$, as explained in Subsection III-A, are employed. As mentioned previously, the times $t_{f1, f2, f3}$ are the terminal times of the individual jerk segments and they satisfy

$$t_{f1} = T_1, \quad t_{f2} = T_3 - T_2, \quad t_{f3} = t_{f1} = T_5 - T_4.$$

The velocities at the concatenation points T_1, \dots, T_5 can be derived to be

$$\begin{aligned} v(T_1) &= v_{f1}, \\ v(T_2) &= v_{f1} + t_1 \cdot a_{\max}, \\ v(T_3) &= v_{f1} + t_1 \cdot a_{\max} + v_{f2}, \\ v(T_4) &= v_{f1} + t_1 \cdot a_{\max} + v_{f2} - t_2 \cdot a_{\max}, \\ v(T_5) &= v_{f1} + t_1 \cdot a_{\max} + v_{f2} - t_2 \cdot a_{\max} - v_{f3}. \end{aligned} \quad (12a)$$

Moreover, the respective positions are given by

$$\begin{aligned} s(T_1) &= s_{f1}, \\ s(T_2) &= s_{f1} + \int_0^{t_1} v(\tau) d\tau = s_{f1} + t_1 \cdot v_{f1} + \frac{1}{2} a_{\max} \cdot t_1^2, \\ s(T_3) &= s(T_2) + (v_{f1} + t_1 \cdot a_{\max}) \cdot t_{f2} + s_{f2}, \\ s(T_4) &= s(T_3) + (v_{f1} + t_1 \cdot a_{\max} + v_{f2}) \cdot t_2 - \frac{1}{2} a_{\max} \cdot t_2^2, \\ s(T_5) &= s(T_4) + s_{f3} = z(t_{f,t}). \end{aligned}$$

Therefore, using $s_f = s_{f1} + s_{f2} + s_{f3}$, the final position is:

$$\begin{aligned} z(t_{f,t}) &= s_f + v_{f1} t_{f2} + t_1(v_{f1} + a_{\max}(t_{f2} + t_2)) + \dots \\ &\quad t_1^2 \frac{a_{\max}}{2} + t_2(v_{f1} + v_{f2}) - t_2^2 \frac{a_{\max}}{2}. \end{aligned} \quad (14)$$

From (12a) and $v(T_5) = 0$, it follows, that

$$v(T_5) = 0 = v_{f1} + t_1 \cdot a_{\max} + v_{f2} - t_2 \cdot a_{\max} - v_{f3}. \quad (15)$$

Solving (15) for t_2 and inserting into (14) leads to

$$0 = t_1^2 + p \cdot t_1 + q$$

with

$$\begin{aligned} p &= \frac{a_{\max} t_{f2} + 2 v_{f1} + v_{f2}}{a_{\max}}, \\ q &= -\frac{z(t_{f,t})}{a_{\max}} + \frac{s_{f1} + s_{f2} + s_{f3} + v_{f1} t_{f2}}{a_{\max}} + \dots \\ &\quad \frac{(v_{f1} + v_{f2} + v_{f3}) \cdot (v_{f1} + v_{f2} - v_{f3})}{2 a_{\max}^2}. \end{aligned}$$

This allows to solve for t_1 directly. From the two possible solutions for t_1 , the smaller one, which is always negative, is ignored. Therefore, the time t_1 is calculated with:

$$t_1 = -\frac{p}{2} + \sqrt{\frac{p^2}{4} - q}. \quad (17)$$

For small transition distances q may be negative which results in negative values for t_1 . This leads to overlapping jerk segments, which, however, can be a viable solution. A detailed discussion of this case, which is illustrated in Figure 8 and Figure 9, can be found in Subsection III-E. Having computed t_1 ,

the duration t_2 follows immediately from (15). The resulting trajectory is checked and it is calculated, if one of the other cases (Case 2 or Case 3) would be the actual solution. This is explained in further detail in Algorithm 1 in Appendix A.

C. Case 2

This case has to be considered, if the kinematic velocity constraint would be violated in Case 1 (see Algorithm 1 in Appendix A). The general shape of the solution is shown in Figure 6. It consists of overall seven individual segments, and can be divided into an acceleration phase on the interval $[0, T_3]$, followed by a constant velocity phase on $[T_3, T_4]$ with duration $t_{v-\max} = T_4 - T_3$, and, finally, a deceleration phase on $[T_4, T_7]$. Therein the acceleration phase is composed of three segments, a jerk segment on the interval $[0, T_1]$, a segment of constant acceleration on $[T_1, T_2]$ and another jerk segment on $[T_2, T_3]$. Similarly, the deceleration phase consists of a jerk segment on the interval $[T_4, T_5]$, a segment of constant acceleration on $[T_5, T_6]$ and another jerk segment on $[T_6, T_7]$.

First, the time at maximal acceleration a_{\max} to reach v_{\lim} results from

$$v_{\lim} = v_{f1} + v_{f3} + a_{\max} t_{a-\max},$$

with the abbreviation $t_{a-\max} = T_2 - T_1 = T_6 - T_5$ and the velocity differences v_{f1} and v_{f3} according to Subsection III-A. This yields

$$t_{a-\max} = \frac{v_{\lim} - (v_{f1} + v_{f3})}{a_{\max}}. \quad (18)$$

Note that high acceleration limits a_{\max} may imply $v_{f1} + v_{f3} > v_{\lim}$ which would result in $t_{a-\max} < 0$ and, therefore, intersecting segments, i.e., $T_2 < T_1$. This is discussed later in this section (cf. also Figure 9 in Subsection III-E). From the considerations in Subsection III-A the symmetry

$$\ddot{z}(t + T_4) = -\ddot{z}(t), \quad t \in [0, T_3]$$

can be deduced, which, together with $\dot{z}(T_4) = v_{\lim}$, implies

$$\dot{z}(t + T_4) = v_{\lim} - \dot{z}(t) \quad (19a)$$

$$z(t + T_4) = z(T_4) + t v_{\lim} - z(t), \quad t \in [0, T_3]. \quad (19b)$$

Denote by $s_{\text{acc}} = z(T_3)$ and $s_{\text{dec}} = z(T_4 + T_3) - z(T_4)$ the total distances travelled during the acceleration and deceleration phases, respectively. According to (19b) these distances satisfy

$$s_{\text{acc}} + s_{\text{dec}} = v_{\lim} T_3 = v_{\lim} \cdot (2 \cdot t_{f1} + t_{a-\max}).$$

For the sake illustration, this relation and the underlying symmetries (19) have been visualized in Figure 6. As a consequence of the above, the final position $z(t_{f,t})$ reached is given by

$$z(t_{f,t}) = v_{\lim} t_{v-\max} + v_{\lim} \cdot (2 \cdot t_{f1} + t_{a-\max}).$$

Therefore, for a given target position, the time spent at maximum velocity v_{\lim} reads

$$t_{v-\max} = \frac{z(t_{f,t}) - v_{\lim} \cdot (2 \cdot t_{f1} + t_{a-\max})}{v_{\lim}}. \quad (20)$$

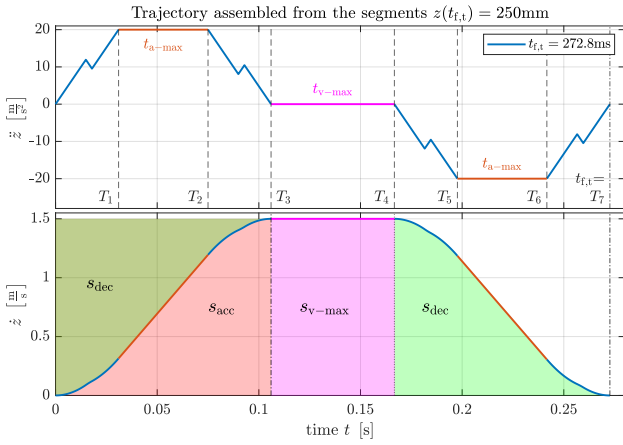


Fig. 6: OCP-J trajectory for Case 2.

D. Case 3

There are certain situations (travelling distances) where neither Case 1 nor Case 2 applies. For these distances the velocity constraint is violated on the interval $[T_2, T_3]$ when using Case 1. For the same distances the maximal velocity is not reached when using Case 2 which results in $t_{v\text{-lim}} < 0$. The particular travelling distances (for the parameter set and kinematic constraints used in this publication) corresponding to this situation are shown in Figure 4.

In the described situation Case 3 is used for trajectory design. The general shape of the trajectory for this case is shown in Figure 7. It consists of overall six individual segments, and can be divided into an acceleration phase on the interval $[0, T_3]$, directly followed by the deceleration phase on $[T_4, T_7]$, whereas $T_3 = T_4$. Similarly to Case 2 these phases are composed of two jerk segments connected by a constant-acceleration segment. In contrast to Case 2, maximum velocity v_{lim} does not need to be reached. Instead, the duration $T_2 - T_1 = T_6 - T_5 = t_{a\text{-max}}$ of the constant-acceleration segments are computed such that the final position $z(t_f)$ is reached (cf. Figure 7). As a prerequisite, the distances travelled

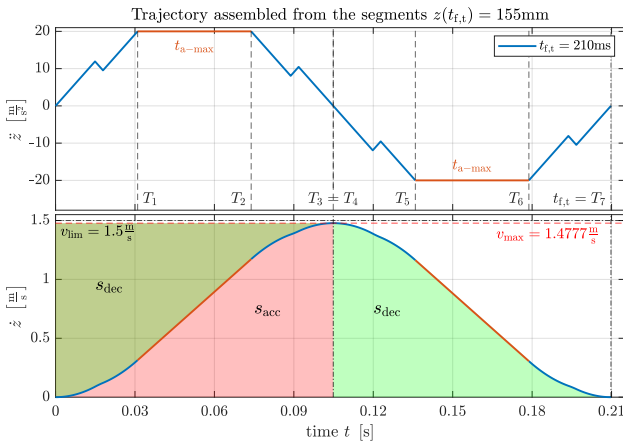


Fig. 7: OCP-J trajectory for Case 3.

during the acceleration and deceleration can be computed by employing the same symmetries as in Case 2 (cf. Figure 7). With $v_{\text{max}} = \dot{z}(T_3)$ the maximum velocity reached, this yields

$$\begin{aligned} z(t_{f,t}) &= v_{\text{max}} \cdot (2 \cdot t_{f1} + t_{a\text{-max}}) \\ &= (v_{f1} + v_{f3} + a_{\text{max}} t_{a\text{-max}}) \cdot (2 \cdot t_{f1} + t_{a\text{-max}}). \end{aligned}$$

Using $v_f = v_{f1} + v_{f3}$ allows to rewrite

$$0 = t_{a\text{-max}}^2 + t_{a\text{-max}} \cdot \underbrace{\frac{2 a_{\text{max}} t_{f1} + v_f}{a_{\text{max}}}}_p + \underbrace{\frac{2 t_{f1} \cdot v_f - z(t_{f,t})}{a_{\text{max}}}}_q.$$

Determining $t_{a\text{-max}}$ by choosing the positive branch of the square-root solution yields

$$t_{a\text{-max}} = -\frac{p}{2} + \sqrt{\frac{p^2}{4} - q}. \quad (22)$$

As in Case 1, $q > 0$ leading to $t_{a\text{-max}} < 0$ is not explicitly excluded.

E. Violation of jerk constraints

As discussed in Subsection III-B, Subsection III-C and Subsection III-D the jerk segments may intersect in certain situations and they are allowed to. However, for particular parameters this overlap may cause a violation of the jerk constraints as shown in Figure 8 and Figure 9. This subsection analyses these violations in more detail and shows how they can be avoided. A reduction of a_{max} is a possibility to avoid these

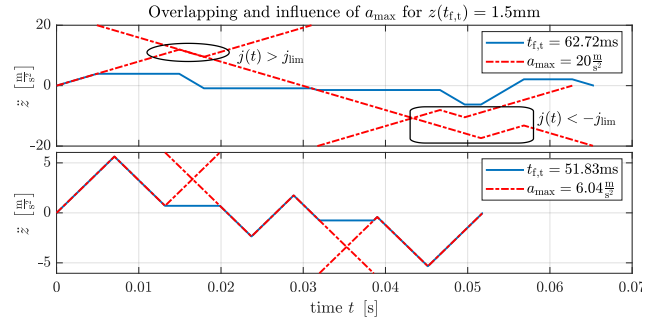


Fig. 8: Superposition of intersecting jerk segments in Case 1. Top: original maximum acceleration causes a violation of the jerk constraint. Bottom: Reduced maximum acceleration avoids violation of the jerk constraint and reduces $t_{f,t}$.

violations, as shown in Figure 8 and Figure 9. This is outlined in Algorithm 3. For the considered parameter set, a detailed analysis of the influence of the maximum acceleration a_{max} on the transition time and the violation of the jerk constraint is shown in Figure 10. Regions corresponding to a violation of the kinematic constraints are hatched. This overview suggests, that there is an optimal acceleration for each distance. When using the proposed design method, it is advantageous to use the ideal acceleration instead of the highest possible acceleration. Since the optimal feasible acceleration a_{max} depends on the travel distance, the calculation of the jerk segments has to

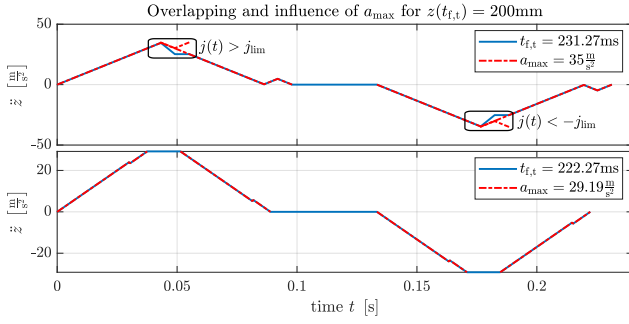


Fig. 9: Superposition of intersecting jerk segments in Case 2. Top: original maximum acceleration causes a violation of the jerk constraint. Bottom: Reduced maximum acceleration avoids violation of the jerk constraint and reduces $t_{f,t}$.

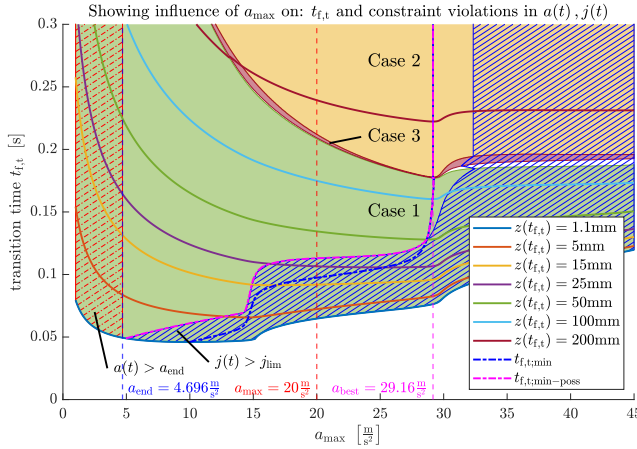


Fig. 10: Influence of a_{\max} on $t_{f,t}$.

be implemented in an efficient manner. An efficient algorithm for the solution of this optimal control problem is presented in [42]. As highlighted by Figure 10, there is a region where very low accelerations a_{\max} can lead to $a(t) > a_{\max}$ for the finished trajectory as shown in Figure 11. For the parameters

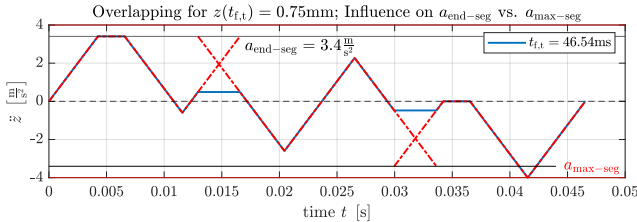


Fig. 11: Trajectory showing, that $a(t) < a_{\text{lim}} = 20 \text{ m/s}^2$, even though $a(t) > a_{\max}$.

presented here, this only occurs for very low accelerations a_{\max} . In particular, for the example depicted in Figure 11, the constraint a_{lim} is satisfied although \ddot{z} exceeds a_{\max} . A method to calculate the ideal acceleration for Case 2: $a_{\max} = a_{\text{best}}$ as marked in Figure 10 is outlined in Section IV.

IV. OPTIMIZING THE FULL TRAJECTORY

As mentioned in Subsection III-E and shown in Figure 10, adjustments of the maximal acceleration a_{\max} used for planning of the jerk segments can lead to an overall reduction of transition times. This motivates the higher-level optimization problem considered in this section. It is thereby assumed that for given maximal acceleration a_{\max} , the overall trajectory is calculated according to Section III. Based on that, the total transition time $t_{f,t}$ is optimized with respect to a_{\max} as the scalar optimization variable. The calculation is developed in detail for Case 2, while a detailed analysis of the remaining cases is postponed to future work.

A. Ideal acceleration a_{\max} for Case 2

The total transition time for the overall trajectory in Case 2 is

$$t_{f,t} = 4 \cdot t_{f1} + 2 \cdot t_{a-\max} + t_{v-\max}$$

with t_{f1} being the terminal time of a single jerk segment, $t_{a-\max}$ the time at maximum acceleration and deceleration and $t_{v-\max}$ the time at maximum slider velocity (see Figure 6). Using (18) and (20) leads to

$$t_{f,t}(a_{\max}) = \frac{z(t_{f,t})}{v_{\text{lim}}} + \frac{v_{\text{lim}}}{a_{\max}} + 2 t_{f1}(a_{\max}) - \frac{v_{f1}(a_{\max}) + v_{f3}(a_{\max})}{a_{\max}}.$$

Searching for the optimal a_{\max} to minimize $t_{f,t}$ is a static optimization problem and the extrema (local minimum or maximum) satisfy

$$\frac{d}{da_{\max}} t_{f,t}(a_{\max}) = 0.$$

Differentiating $t_{f,t}(a_{\max})$ with regards to a_{\max} in order to minimize $t_{f,t}(a_{\max})$ gives

$$\frac{1}{a_{\max}^2} \left[2 a_{\max}^2 \frac{d}{da_{\max}} t_{f1}(a_{\max}) + v_{f1}(a_{\max}) + v_{f3}(a_{\max}) - v_{\text{lim}} - a_{\max} \cdot \frac{d}{da_{\max}} (v_{f1}(a_{\max}) + v_{f3}(a_{\max})) \right] = 0 \quad (23)$$

Solving (23) for a_{\max} gives the optimal acceleration a_{best} for Case 2. This confirms, that the optimal acceleration for Case 2 is independent of the transition distance as suggested by the results shown in Figure 10. However, as Case 2 can only be used on a certain interval of distances as shown in Figure 4, the optimal value for a_{\max} may still depend on the transition distance. The result for the derivation of $t_{f,t}(a_{\max})$ is plotted in Figure 12. The result shows, that there exists several local optima, at least for the particular parameters used here.

B. Optimal maximum acceleration for Cases 1 and 3

In contrast to Case 2, the optimal a_{\max} for Cases 1 and 3 also depend on the overall transition distance, because of the terms $z(t_{f,t})/a_{\max}$ in (17) and (22) respectively. As Figure 10 suggests, the ideal acceleration for Case 1 and Case 3 can be slightly higher or lower than the ideal acceleration obtained for Case 2. This is underlined by Figure 13, which shows the results of a more detailed numerical analysis. Here the globally optimal a_{\max} was evaluated and the transition time is

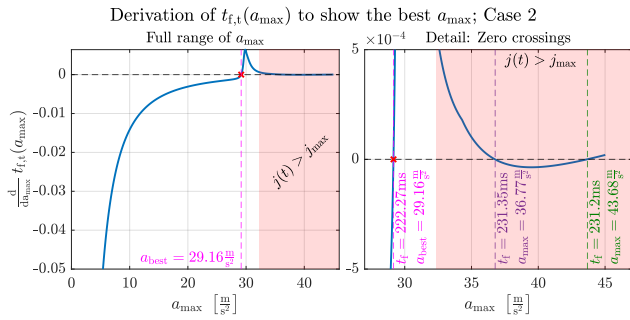


Fig. 12: Best acceleration for this set of parameters (Case 2).

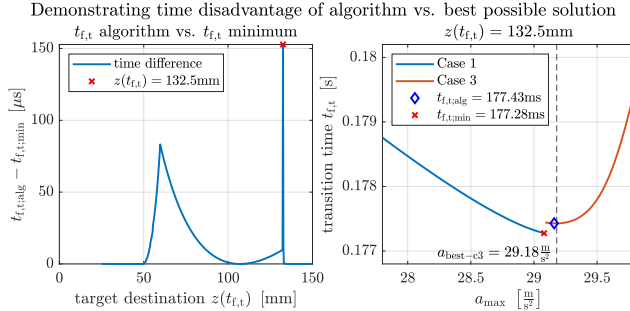


Fig. 13: Applying the algorithm to the trajectories and comparing the transition times with the best possible transition times to show the effectiveness of the algorithm (specific for distance).

compared to the transition time achieved with the algorithm described in Appendix A. This result shows, that for a certain range of distances the result of the algorithms described below could be further improved. As the result in Figure 13 shows, the potential for improvement for the parameter set considered here is below 200 μs , which is smaller, than a single PLC cycle. For this reason, it was postponed for future work.

V. COMPARISON WITH EXISTING METHODS

This section is devoted to a comparison with established and recently developed trajectory planning methods. Trajectories are compared w.r.t. transition times, parameter sensitivity and general limitations are listed. First, the trajectory planning approaches are briefly explained in Subsection V-A. Afterwards the parameters from Table I and the kinematic constraints from Table II are used to demonstrate the performance characteristics of the OCP-J approach in Subsection V-B. These are the parameters that most closely resemble the production machines, and are therefore used to highlight the performance that can be expected in a real-world setting. Additional parameter sets (one from the laboratory system used for validation and one from [40]) are taken and the performance of the OCP-J approach is shown for these parameter sets. This analysis and the parameters are given in Subsection V-C.

A. Planning approaches considered in comparison

A regular S-Curve [19], that does not consider any oscillation of the system, is used as a baseline. This trajectory represents the fastest way to reach an endpoint, taking into account all kinematic constraints of the actuator (velocity, acceleration and jerk), but not the system's internal dynamics. The second trajectory planning approach, is the ZV-shaped S-Curve [25], [23], a well established method in the field and has been shown to work very well [54]. This approach was chosen for comparisons over more involved shapers [52], [31], [30], [6], [18], [24], [20] because it represents the fastest positive impulse shaper [25], [23]. Due to the nature of negative impulse shapers [27], [1], kinematic constraints may be violated (although there are strategies to avoid violation [1]), they are not included in the comparison. The third method is the OCP-S approach [34], [38], [44], [49], [3], outlined in Subsection II-C, which uses full discretisation to solve the trajectory planning problem in a time-optimal manner. The fourth approach is an implementation of an improved FIR filter as given in [40]. It is denoted FIR_{Imp} in the figures. It is an improved version of [8], [10], [47], an implementation of which can be found in [45]. For the third order trajectories (limited jerk, continuous acceleration, velocity and position), [8], [2], [10], [47], [45], [40] is a variation of [7], [13], [21] which allows a further reduction of the transition time in selected cases at the expense of parameter sensitivity. A direct comparison with [7], [13], [21] would therefore be redundant. Approaches that also consider derivatives of the jerk [28], [9], [16] are not included because they were developed for a different purpose and would therefore not provide the best comparison. Since [40] is a further development of [47] that helps to remove violations of kinematic constraints, it was chosen for the comparisons instead of [47].

B. Comparison with parameters presented here

For the first comparison, the parameters from Table I and the kinematic constraints from Table II are used to calculate and compare different trajectories. Trajectories for a single distance are shown in Figure 14 (contains the trajectories shown in Figure 2 and in addition the OCP-J and FIR_{Imp} approaches). All of the acceleration profiles start at $a(0) = 0 \text{ m/s}^2$ respectively, but they have been separated by 10 m/s^2 in the plot for better visibility and comparison. Two more specific distances are shown, that are of interest. The first in Figure 15, where the transition time of the OCP-J approach is within 1 ms of the FIR_{Imp} and a second, where the original S-Curve has the same transition time, as the FIR_{Imp} . The amount of time saved or gained depends on the distance and can additionally vary depending on the approach. The ZV-shaped S-Curve is always exactly half an oscillation period slower, than the underlying S-Curve. For the other approaches, the time saved varies relative to a ZV-shaper. For this reason, distances between 1 mm and 300 mm were analysed. The result of this is shown in Figure 17, comprising the total transition times and times gained or lost compared to the ZV-shaped S-Curve. The comparison with the ZV shaped S-Curve was

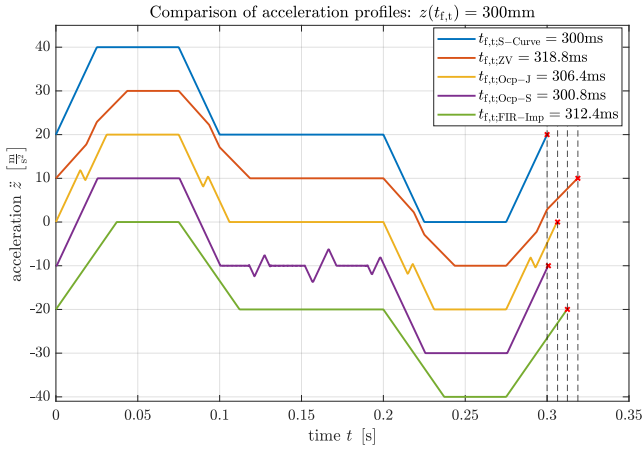


Fig. 14: Trajectories: S-Curve, ZV, OCP-S, OCP-J and FIR_{Imp} for a comparison of transition times for the motion distance $z(t_{f,t}) = 300 \text{ mm}$.

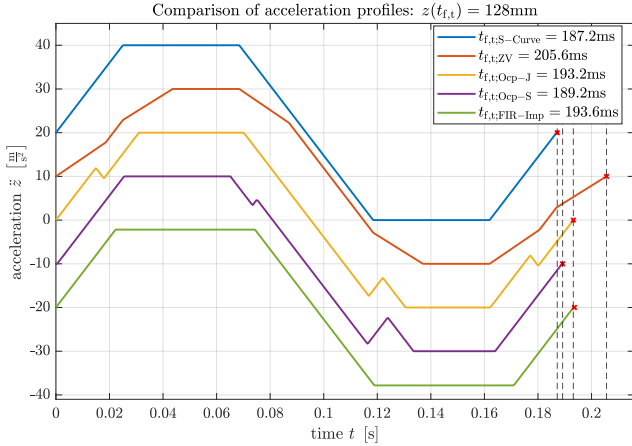


Fig. 15: Trajectories: S-Curve, ZV, OCP-S, OCP-J and FIR_{Imp} for a comparison of transition times for the motion distance $z(t_{f,t}) = 128 \text{ mm}$.

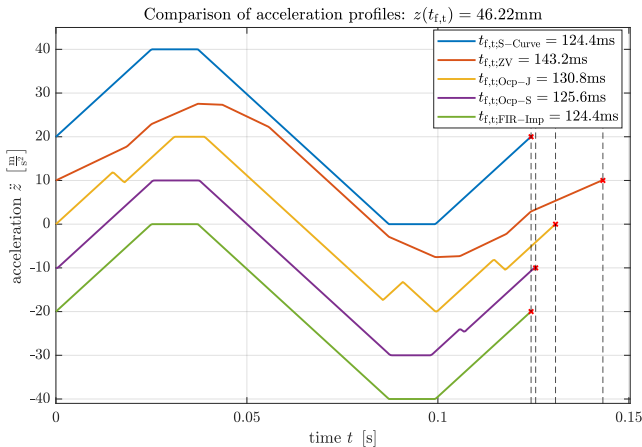


Fig. 16: Trajectories: S-Curve, ZV, OCP-S, OCP-J and FIR_{Imp} for a comparison of transition times for the motion distance $z(t_{f,t}) = 46.22 \text{ mm}$.

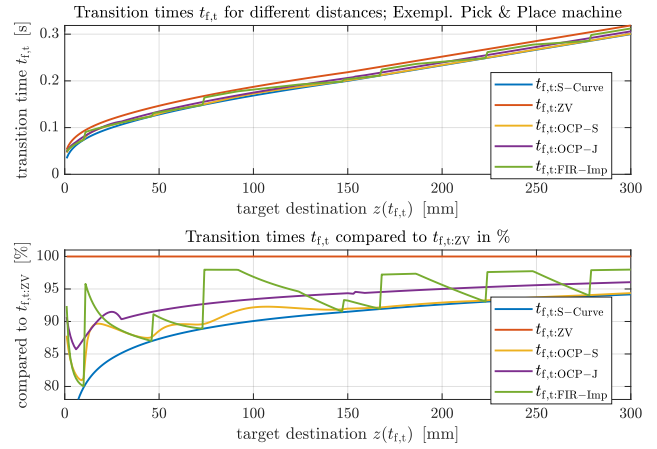


Fig. 17: Transition times for all methods. Shown are the absolute times and the times relative to the ZV-shaper. The comparison is made to the ZV-shaper, because it is the established method (plot not taken from [4]).

chosen because it is a widely used and universally applicable technique. The approaches ZV, OCP-S and OCP-J approaches allow damping to be taken into account, while FIR_{Imp} does not. Whenever the system response to a trajectory exhibits oscillation, the amplitude is determined using the method shown in Figure 18. An envelope is fitted on the decaying oscillation and the resulting amplitude at $t_{f,t}$ (end of the slider movement) is evaluated and labelled with a_0 , as shown in the plot. In Figure 18 the slider acceleration for a FIR_{Imp} trajectory is shown together with the system response for two systems. First, the system response for a system without damping ($d = 0$) is shown to demonstrate, that oscillation-free transitions can be achieved for those systems as mentioned in [40]. Secondly, the system response with the actual damping from Table I is shown to show the influence of the neglected system damping. Another comparison for the same distance,

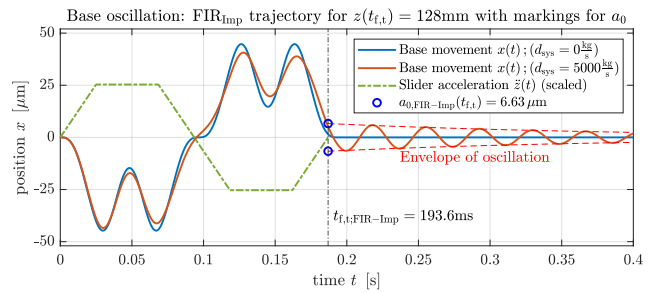


Fig. 18: Oscillation in base to mark, where and how the oscillation a_0 for a FIR_{Imp} trajectory is determined.

but for the OCP-J trajectories developed in this contribution, is shown in Figure 19. As this approach can take damping into account, the trajectories calculated for the system with and without damping are different. The possibility of taking system damping into account in the OCP-J approach opens the possibility to use it on system with damping.

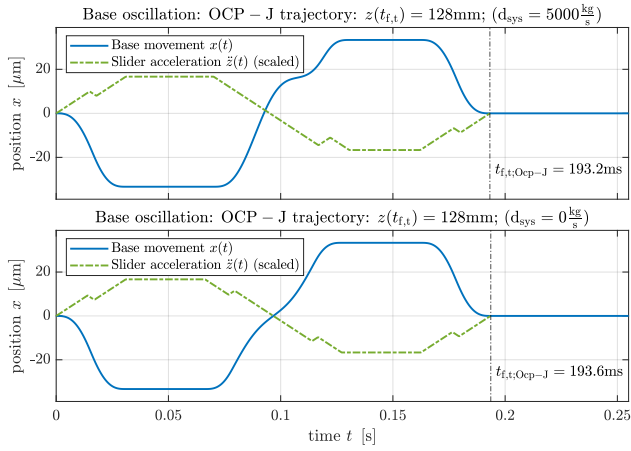


Fig. 19: Oscillation in base to mark, where and how the oscillation a_0 for a OCP-J trajectory is determined.

C. Comparison for different parameters

To give a broader analysis and show the performance w.r.t. transition time (and also parameter uncertainty), comparisons with additional parameter sets are provided. All parameter sets are summarized in Table III. The abbreviation *Ex.-PaP.* stands for parameter set of exemplary pick and place machine which are given in Table I and Table II. The corresponding results are shown in Figure 17. The parameters *Set: [40]* are the parameters used in [40] for the distance sweep. The last abbreviation *Lab.-Sys.* marks the parameters of the laboratory system used for the measurements (more details for this system follow in Section VI). In the table ω_0 refers to the angular eigenfrequency and $\delta = d/2 \cdot m_g$ refers to the damping of the system. The analysis shown in Figure 17 has been

TABLE III: All parameter sets listed for overview

Param-Set	$v_{lim} [\frac{m}{s}]$	$a_{lim} [\frac{m}{s^2}]$	$j_{lim} [\frac{m}{s^3}]$	$\omega_0 [\frac{rad}{s}]$	$\delta [\frac{1}{s}]$
Ex.-PaP.	1.5	20	800	169.03	4.762
Set from: [40]	1	2	10	40	0
Lab.-Sys.	0.45	6	200	61.02	0.799

repeated for the additional parameters listed in Table III. The transition times relative to the ZV-shaped trajectory are shown in Figure 20. In analysing these results, some observations can be made which are summarised in the discussion (Section VII) together with the results of the rest of this section.

D. Analysis of parameter sensitivity

The previous section showed the transition times for the different trajectory planning approaches. Another important issue to be considered is the sensitivity of the approaches w.r.t. parameter uncertainty, which is analysed in this subsection. To this end, the trajectories are all calculated for the nominal parameters shown in Table I with the kinematic constraints from Table II. In the analysis ω_d is adjusted to show the residual amplitude of oscillation under parameter uncertainty. The method used to determine this amplitude is illustrated

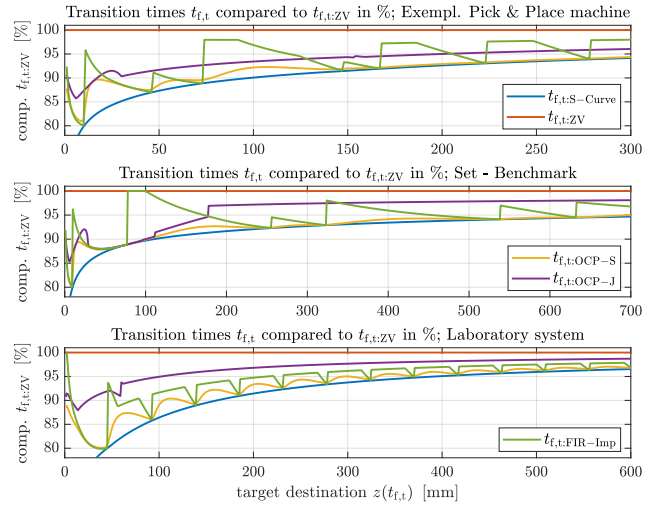


Fig. 20: Transition times relative to the ZV-shaper for all of the parameter sets from Table III.

in Figure 18. The sensitivity to parameter uncertainty for the trajectories from Figure 14-16 is shown in Figure 21. Another analysis for the parameter set of the laboratory system is shown together with measurements in Section VI. Note that an uncertainty in the oscillation frequency of 10% corresponds to about a 20% error in the measured system stiffness k . Note that the area under consideration is larger than it would be in practice just to visualize the behaviour under larger uncertainties. All of the results are summarily discussed in

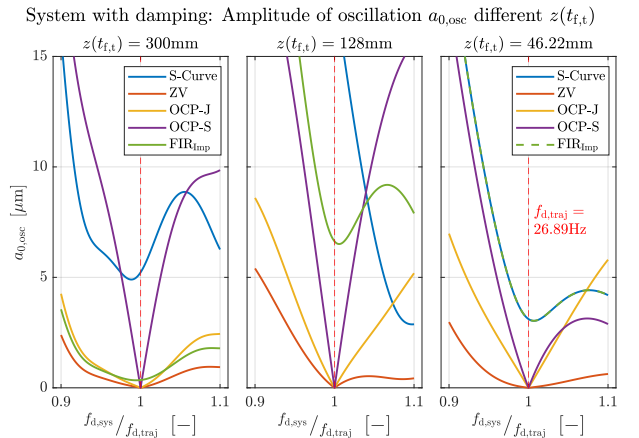


Fig. 21: Sensitivity to parameter uncertainty: Comparison of approaches for the distances shown in Figure 14, Figure 15 and Figure 16.

Section VII.

VI. EXPERIMENTS ON LABORATORY SYSTEM

This section describes the experiments carried out on a laboratory system to validate the approach. The laboratory system and parameter combinations are given and an implementation aspect is mentioned. The planning methods

presented in Section V are implemented (except for OCP-S; see: Subsection II-C) on the PLC. The trajectories shown in the measurement have been calculated directly on the PLC. Measurements have been performed for the different methods, for different distances and parameter combinations.

A. Laboratory setup

A CAD-picture of the laboratory system is shown in Figure 22. The base movement $x(t)$ from Figure 1 corresponds to the position of the main carriage mounted between the two springs and $z(t)$ to the slider mounted on the bottom of the test rig (both the left and rightmost position of the slider are shown in the picture). In order to study the influence of parameter uncertainty on trajectory planning approaches, the springs are easily interchangeable. Replacing the springs also alters the damping of the system and the five sets of parameters (cf. [43]) are listed in Table IV, where configuration 3_{nom} is the parameter set all for which all trajectories were planned. It is

TABLE IV: Parameters of the system: Changes in stiffness to show effect of parameter variation (table taken from [43]).

N_{sys}	k_{sys}	d_{sys}	$f_{d,\text{sys}}$
1	$k_1 = 94\,583\text{ N/m}$	$d_1 = 68.1\text{ kg/s}$	$f_{d,\text{sys},1} = 8.71\text{ Hz}$
2	$k_2 = 105\,532\text{ N/m}$	$d_2 = 67.2\text{ kg/s}$	$f_{d,\text{sys},2} = 9.2\text{ Hz}$
3 _{nom}	$k_{\text{traj}} = 117\,499\text{ N/m}$	$d_{\text{traj}} = 50.4\text{ kg/s}$	$f_{d,\text{traj}} = 9.71\text{ Hz}$
4	$k_4 = 131\,367\text{ N/m}$	$d_4 = 54.3\text{ kg/s}$	$f_{d,\text{sys},4} = 10.27\text{ Hz}$
5	$k_5 = 140\,042\text{ N/m}$	$d_5 = 56.9\text{ kg/s}$	$f_{d,\text{sys},5} = 10.601\text{ Hz}$

important to note, that the influence of parameter uncertainty is shown for comparison only. As mentioned previously, the trajectory planning approach has not been specifically optimized for behaviour under parameter uncertainty. In reality, some small uncertainty in the system is unavoidable so some level of robustness to parameter uncertainty is required.

B. Implementation and computational complexity

This section outlines how the required code can be implemented on the PLC and explains why the presented method was chosen. The implementation for the full trajectories presented in Section III and Section IV is best split into three separate functions when implementing to avoid unnecessary duplication of code. The three parts are given in Appendix A. The first part given in Algorithm 1 implements the equations shown in Section III and returns the OCP-J trajectory based on a given a_{max} . This a_{max} is provided by the overlying function incorporating Algorithm 2. After a trajectory is returned by Section III, the calculations from Algorithm 2 check if any kinematic constraints are violated. This happens for very small distances due to the large negative overlap of the jerk segments mentioned before (see Figure 8 or Figure 9). If a violation of the kinematic constraints occurs in Algorithm 2, the last method shown in Algorithm 3 is used to optimize a_{max} to resolve these violations and to ensure minimal transition times (it is known that this can happen and has been taken into account). Performing the calculation in this way ensures that the trajectory respects the kinematic constraints and that the transition times are as small as possible with the OCP-J

(cf. Section IV). Two additional details are provided in the following. First, the computational complexity is addressed, and subsequently, a post-processing step is outlined, necessary to provide the trajectory on the discrete controller intervals.

1) *Computational complexity and calculation times:* For the parameters and kinematic constraints given in Table I and Table II, the part of the algorithm to adjust a_{max} (Algorithm 3) only needs to be called for transition distances $z(t_{f,t})$ less than 30 mm. For distances above this limit, the calculation of a complete trajectory is finished after calling Algorithm 1 once. Note that the calculation of the required jerk segments is completed after a fixed number of steps as well (the first two steps in Algorithm 1 and the method is as described in [42]). For transition distances below this limit, the computational effort is higher because Algorithm 3 is executed. The total number of steps in Algorithm 3 can vary depending on which of the two terminal conditions (as explained in Appendix A) is triggered first. In the worst case, the calculation is called $n_{\text{max,iter}}$ times. It turned out that using single precision on the PLC is sufficient, as the measurement results in Subsection VI-C show.

To demonstrate the frequency of adjustments of a_{max} and to show real computation times, trajectories were planned for different distances. The resulting optimal values for a_{max} and the total computation times are shown in Figure 23. The times were measured on a regular PC (i7-1185G7 processor and code running in MATLAB) and on a PLC (X20CP1585 and code programmed in structured text). Both times are shown in Figure 23. This shows, that adjustments of a_{max} are required only for small overall distances (below 30 mm for the given parameters). Note that it is not always possible to work with pre-calculated jerk segments from previous runs, as the process parameters may change due to parameter drift. As Algorithm 1 may be called several times by Algorithm 3, the calculation must be efficient and fast. For this reason, the algorithm presented in [42], which allows efficient calculation of the jerk segments, is advantageous. Listing the number of individual function evaluations are required is not useful, and instead the calculation time required on a PLC are given directly.

2) *Post-processing:* The calculation of the switching times corresponding to jerk changes from j_{max} to 0, $-j_{\text{max}}$ and vice versa is not bound to the specific controller cycle $t_{\text{ctrl}} = 400\text{ }\mu\text{s}$ of the PLC itself. To provide the position controller with the reference trajectory on the specific discrete interval, the equations given in (5) have to be used directly (as the equations show, the computation time required for this step is basically negligible). This step results in rounding the final time of the trajectory $t_{f,t}$ to a full controller cycle. This approach is comparable to the supersampling approach outlined in [19]. It enables the utilization of a continuously computed trajectory to derive a reference trajectory on the discrete controller interval.

C. Measurements

Since simulations of the trajectories under parameter uncertainty were shown, and the test rig specifically allows

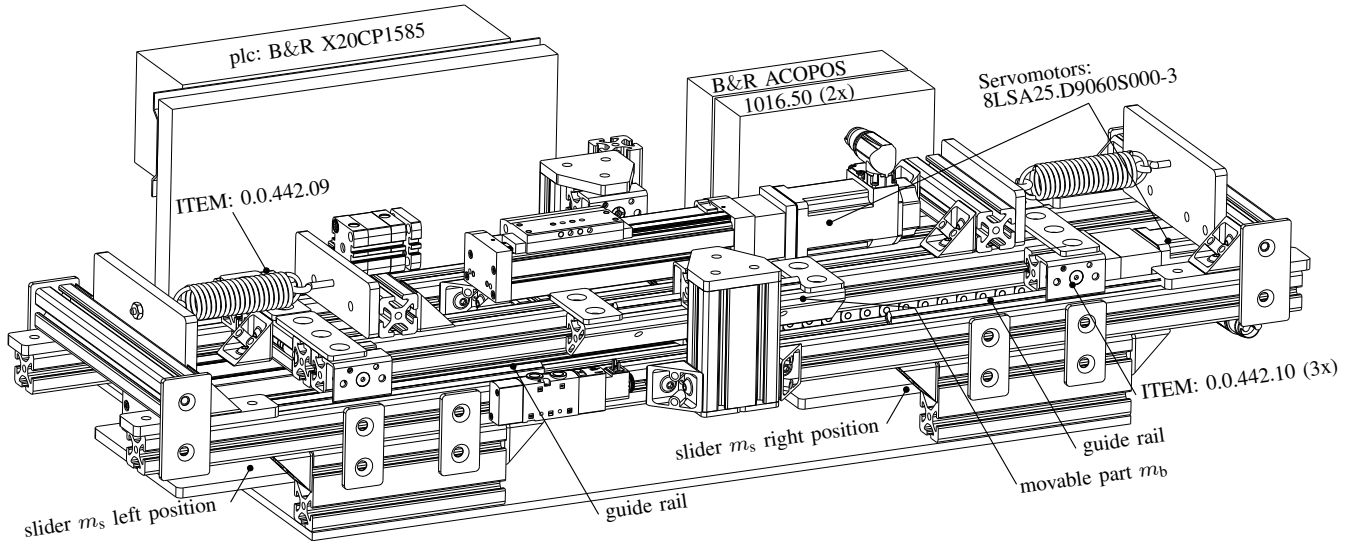


Fig. 22: CAD-picture of the laboratory system used for the measurements (picture also shown in [43]).

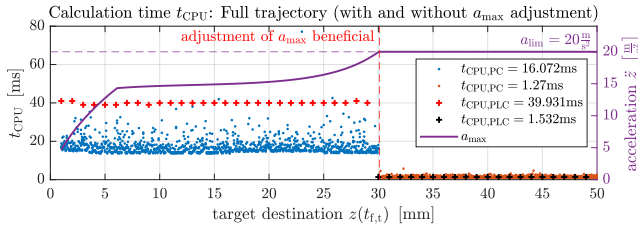


Fig. 23: Showing a_{\max} and t_{CPU} (average times over the points marked) used for different transition distances.

such measurements, measurements were also made for this reason. The depicted results show the amplitude of oscillation occurring after the slider reaches its final position. Here, an oscillation for a small timespan covering 0.25 s or roughly 2 oscillation periods, corresponding to

$$x(t) = a_0 \cdot e^{-\delta(t-t_{f,t})} \sin(\omega_d t - \varphi_0)$$

is fitted to the measurements. This is shown for three measurements in Figure 24-25. The first measurement in Figure 24

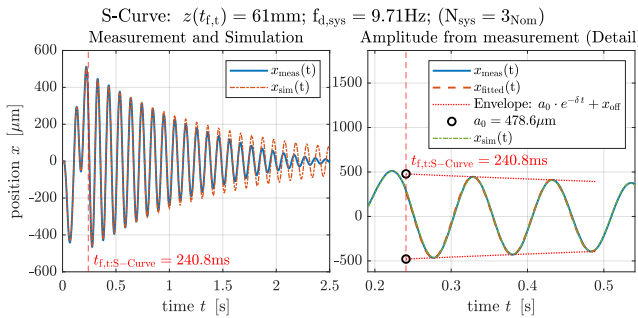


Fig. 24: Measurement of S-Curve trajectory showing oscillation (oscillation of base).

shows the system response to an S-Curve. The second and

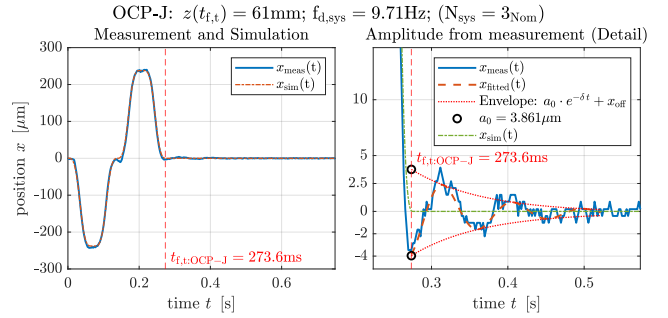


Fig. 25: Measurement of OCP-J trajectory with good system knowledge (oscillation of base).

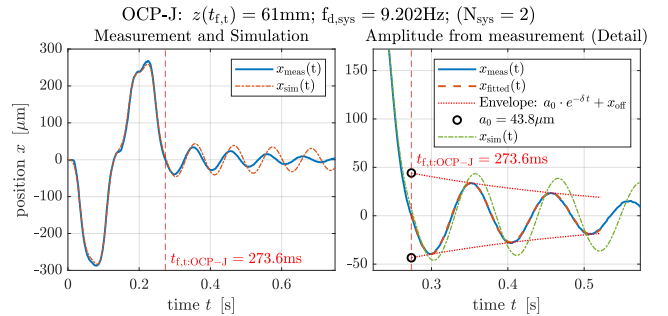


Fig. 26: Measurement of OCP-J trajectory under parameter uncertainty (oscillation of base).

third trajectory show the OCP-J trajectory, planned for the frequency $f_{d,\text{traj}}$ as given in Table IV. The response for a system, where $f_{d,\text{sys}} = f_{d,\text{traj}}$ is shown in Figure 25. The remaining oscillation is due to remaining model inaccuracies. In particular non-linear friction, which most likely occurs in the laboratory setup, is not covered in the model. This assumption is supported by the fact, that (as the plots show) the

oscillation tends to decay quicker, as the amplitude decreases. The system response under larger trajectory parameter uncertainty for the same trajectory is then shown in Figure 26. These measurements were then repeated for five different distances, the five different trajectory planning methods presented and for the system parameters given Table IV. All of the distances, methods and the corresponding transition times are given in Table V.

TABLE V: Transition times $t_{f,t}$ for measured distances and trajectory planning methods.

Transition distance	S-Curve	ZV	FIR _{Imp}	OCP-J
$z(t_{f,t}) = 14.5 \text{ mm}$	132.8 ms	184.4 ms	156.4 ms	162.4 ms
$z(t_{f,t}) = 61 \text{ mm}$	240.8 ms	292.4 ms	260.4 ms	273.6 ms
$z(t_{f,t}) = 116 \text{ mm}$	362.8 ms	414.4 ms	382.8 ms	395.2 ms
$z(t_{f,t}) = 139 \text{ mm}$	414 ms	465.6 ms	414 ms	446.4 ms
$z(t_{f,t}) = 181 \text{ mm}$	507.6 ms	558.8 ms	515.2 ms	539.6 ms

Plots similar to Figure 21 show a comparison of simulated amplitudes and the measurements. These plots serve a dual purpose. First, they show the behaviour of the planned trajectories under parameter deviation (similar to Figure 21). Secondly, a comparison of the measured and simulated amplitudes is shown in the plots, where all measurements and the deviation between simulated and measured amplitudes are visible. The simulated amplitudes are the solid lines in the plots. The measurements correspond to the small bars located at the different frequencies. Each measurement was repeated five times and the minimal and maximal amplitudes are given in Table VI located in Appendix B. The measurements for the first distance of Table V are shown in Figure 27. The full picture of the measurements is shown on the left of the plot and a detail for a smaller range of amplitudes and system frequencies is shown on the right. The same is shown for the rest of the distances in Figure 28 and the details in Figure 29. The measurements, a comparison to the simulation

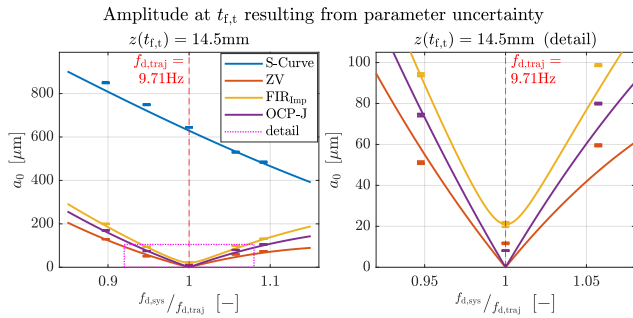


Fig. 27: Overview of all measurements and simulated amplitudes under parameter uncertainty (on distances with detail).

results and the trajectory planning method are next discussed in Section VII.

VII. DISCUSSION OF RESULTS

The selection of methods has already been discussed in Subsection V-A. As the results from Figure 20 show, the

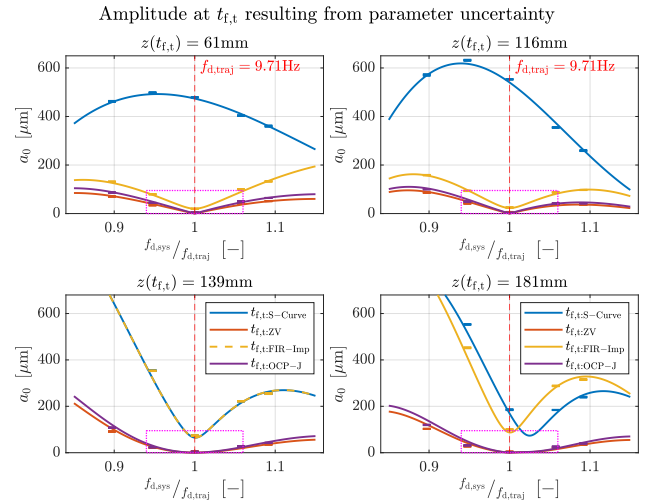


Fig. 28: Overview of all measurements (four distances) and simulated amplitudes under parameter uncertainty (marked details shown in Figure 29).

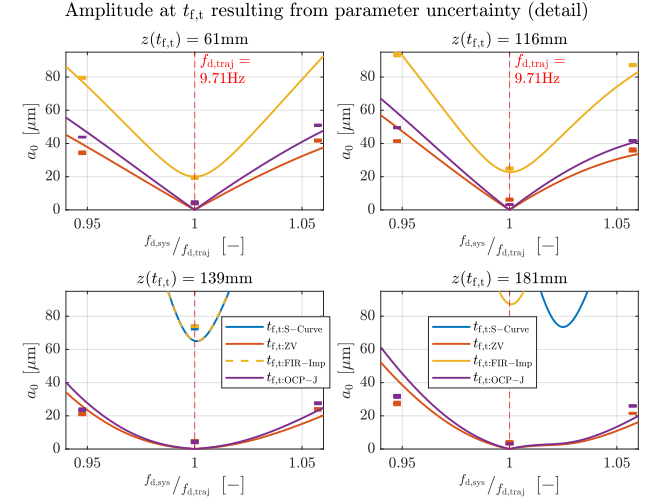


Fig. 29: Overview of all measurements (four distances) and simulated amplitudes under parameter uncertainty (details for measurement shown in Figure 28).

methods presented offer slightly faster transitions than ZV shaping at the expense of increased parameter sensitivity. Since small uncertainties in the model and parameters are unavoidable, the analysis of the approaches w.r.t. parameter uncertainty was included. It is important to note however, that none of the methods presented is specifically adapted to parameter uncertainty. For OCP-S, the mathematical formulation only ensures, that the internal dynamic is at rest at the end of the transition. For OCP-J, the system is (with perfect system knowledge) oscillation free, whenever hitting $\pm a_{\max}$ and v_{\max} respectively. In other words, the reduces sensitivity to parameter uncertainty the OCP-J results from the fact, that all oscillations are cancelled in the jerk-phase of the trajectory. For the ZV-shaped trajectory, every oscillation induced in

the system is always cancelled half of an oscillation period later, leading to the even better behaviour w.r.t. parameter uncertainty. For FIR_{Imp} this is not the case, as (for the third-order trajectories shown here) oscillation can be removed by the spacing of three different times, depending which is fastest, as explained in [40]. The OCP-J approach was developed specifically to be able to take system damping into account, as it is possible with ZV-shaping.

The possibility of taking system damping into account allows to plan trajectories with significantly smaller oscillation, as the measurement shown in Section VI demonstrates. Note, that the method also applies to systems without damping. Considering the small stiffness of the laboratory system, when comparing to an actual pick-and-place machine the practicality of the OCP-J was demonstrated. Measurement results shown in Figure 24 and Figure 25 show the substantial reduction in oscillation amplitude, if the system parameters are known with a high degree of accuracy. The system response under parameter uncertainty of the ZV-shaped S-Curve and the OCP-J trajectories are further quite similar, as demonstrated with the measurements shown in Figure 27, Figure 28 and Figure 29.

A detailed analysis of time improvement for different sets of parameters is provided in Figure 20. It is important to note, that the OCP-J approach aims at a specific problem, where very low oscillation in a short amount of time has to be achieved. The measurements and simulation results for the exemplary pick-and-place machine shown in Figure 21 underline the usefulness of the approach. In this publication, we emphasised and focused comparisons to ZV-shaping. It is an established approach, that works exceptionally well [54], most crucially allows to take system damping into account and is simple to implement. Recent developments, like the original FIR approach [8], [10], [47] and the newer FIR_{Imp} [40] allow for a reduction of transition times, at the expense of stability to parameter uncertainty, as shown in Figure 21. For highly accurate pick-and-place systems we consider the OCP-J approach to be a the better alternative, because damping can be taken into account.

Although a model of a pick-and-place system has been used to develop the trajectory planning approach, in the end it is only influenced by the system oscillation frequency ω_d , the system damping δ and the kinematic constraints of the actuator. The latter are the maximum velocity v_{lim} , the acceleration a_{lim} and the jerk j_{lim} . In other words, if ZV-shaping can be used(/is currently in use on a system), the OCP-J approach is also applicable. The system parameters have to be measured and the kinetic constraints of the actuator usually come from the drives themselves (especially v_{lim} and a_{lim}). It is recognised that higher jerk j_{lim} usually leads to higher vibration [5], [48] and higher wear [26], [55]. For this reason, the limit for jerk is usually based on previous experience on a system and can be set and adjusted by analysing the system response and the tracking behaviour of the slider on a trajectory. If tracking is

poor (resulting in higher residual oscillation), the jerk needs to be reduced. If tracking is satisfactory, the jerk can be increased, resulting in a reduction of transition times. A reasonable limit for the jerk to start (in the absence of prior experience) can be given as follows

$$j_{lim,init} = \frac{a_{max} \cdot \omega_d}{2\pi}.$$

By analysing the system's response to this jerk using the method described above, it is possible to make adjustments until a satisfactory result is reached (see also Figure 25).

VIII. SUMMARY AND OUTLOOK

A. Summary

A method for planning trajectories called OCP-J based on motion primitives (called jerk segments) was introduced and its effectiveness in terms of transition time and parameter uncertainty was analysed on a laboratory system. It was found that recalculating the jerk segments with acceleration levels lower than the physical maximum has a positive effect on the transition time and helps to remove violations of kinematic constraints. This led to the development of an efficient algorithm to compute the segments published in [42]. The presented calculation method allows implementation on a PLC (which was done) without relying on any optimization libraries. As the comparisons Figure 23 and Figure 17 show, the calculation time of the trajectories is less than the transition time, even on a system with limited computing power (10 year old CPU on the tested PLC). The fact that the calculation always performs the same steps also leads to known and consistent calculation times. This allows the trajectories to be calculated as they are needed, without the need for pre-calculation. As shown in Figure 20, the OCP-J approach offers a reduction in transition times of between 5% and 10% compared to the ZV shaping approach.

B. Outlook

In future work, it is planned to combine the OCP-J approach with a continuous update of the system parameters, which is made possible by the fast trajectory computation. A detailed analysis of the algorithm used to optimise a_{max} might also allow to solve for the actual best a_{best} for Case 1 and Case 3. In this context, a mathematical proof of what a_{best} is might prove useful for further development of the algorithm. The use of jerk segments specifically optimised for performance w.r.t. parameter uncertainty is planned for the future. Alternatively, adaptation to multiple eigenfrequencies may be considered. Changes to the jerk segments themselves (contents of [42]) will only affect the calculation required for the jerk segments, but the calculation of the full trajectories shown here will remain the same. This is the subject of planned future work.

REFERENCES

- [1] Khalid L. Sorensen, Aayush Daftari, William E. Singhose, and Keith Hekman. Negative input shaping: Eliminating overcurrenting and maximizing the command space. *Journal of Dynamic Systems, Measurement, and Control*, 130(6), oct 2008.
- [2] Pierre Besset and Richard Béarée. Fir filter-based online jerk-constrained trajectory generation. *Control Engineering Practice*, 66:169–180, September 2017.
- [3] Thomas Auer, Phillip Kronthaler, and Frank Woittennek. Optimalsteuerungsentwurf für ein elastisch gekoppeltes Flächenportal mit Vergleich zu Standardverfahren. 7. *IFTOMM D-A-CH Konferenz*, 2021: 18./19. Februar 2021:Online-Konferenz, 2021.
- [4] Thomas Auer and Frank Woittennek. On trajectory design for flexible structures with input and state constraints. *IFAC*, 2023.
- [5] Hasti Hayati, David Eager, Ann-Marie Pendrill, and Hans Alberg. Jerk within the context of science and engineering—a systematic review. *Vibration*, 3(4):371–409, October 2020.
- [6] W. E. Singhose, L. J. Porter, T. D. Tuttle, and N. C. Singer. Vibration reduction using multi-hump input shapers. *Journal of Dynamic Systems, Measurement, and Control*, 119(2):320–326, jun 1997.
- [7] P.H. Meckl and P.B. Arestides. Optimized s-curve motion profiles for minimum residual vibration. In *Proceedings of the 1998 American Control Conference. ACC (IEEE Cat. No.98CH36207)*. IEEE, 1998.
- [8] Luigi Biagiotti, Claudio Melchiorri, and Lorenzo Moriello. Optimal trajectories for vibration reduction based on exponential filters. *IEEE Transactions on Control Systems Technology*, pages 1–1, 2015.
- [9] Rupesh Tatte, Hemant Thorat, and Hemant Jawale. Optimization of higher-order s-curve motion profile using unitization method aiming to reduce the vibration of a lightly damped system. *Journal of the Brazilian Society of Mechanical Sciences and Engineering*, 46(4), March 2024.
- [10] Luigi Biagiotti and Claudio Melchiorri. Trajectory generation via fir filters: A procedure for time-optimization under kinematic and frequency constraints. *Control Engineering Practice*, 87:43–58, June 2019.
- [11] Dibakar Bandopadhyaya, Dileep Bhogadi, B. Bhattacharya, and A. Dutta. Active vibration suppression of a flexible link using ionic polymer metal composite. In *2006 IEEE Conference on Robotics, Automation and Mechatronics*. IEEE, December 2006.
- [12] C. D. Porawagama and S. R. Munasinghe. Reduced jerk joint space trajectory planning method using 5-3-5 spline for robot manipulators. In *7th International Conference on Information and Automation for Sustainability*, pages 1–6. IEEE, December 2014.
- [13] Richard Béarée. New damped-jerk trajectory for vibration reduction. *Control Engineering Practice*, 28:112–120, July 2014.
- [14] Avinash Gopal Dharne and Suhada Jayasuriya. Robust adaptive control of residual vibration in point-to-point motion of flexible bodies. *Journal of Vibration and Control*, 13(7):951–968, July 2007.
- [15] Tarunraj Singh and Tomáš Vyhldal. Recent results in reference prefiltering for precision motion control. *IFAC-PapersOnLine*, 53(2):8656–8667, 2020.
- [16] Chol Jun Han, Kwang Rim Song, and Un-Ryong Rim. An asymmetric s-curve trajectory planning based on an improved jerk profile. *Robotica*, 42(7):2184–2208, April 2024.
- [17] K.J. Kyriakopoulos and G.N. Saridis. Minimum jerk path generation. In *Proceedings. 1988 IEEE International Conference on Robotics and Automation*, pages 364–369. IEEE Comput. Soc. Press.
- [18] N. Singer, W. Singhose, and W. Seering. Comparison of filtering methods for reducing residual vibration. *European Journal of Control*, 5(2-4):208–218, jan 1999.
- [19] Luigi Biagiotti Claudio Melchiorri. *Trajectory Planning for Automatic Machines and Robots*. Springer-Verlag GmbH, October 2008.
- [20] William Singhose. Command Shaping for Flexible Systems: A Review of the First 50 Years. *International Journal Of Precision Engineering And Manufacturing*, 2009.
- [21] Joonyoung Kim and Elizabeth A. Croft. Preshaping input trajectories of industrial robots for vibration suppression. *Robotics and Computer-Integrated Manufacturing*, 54:35–44, December 2018.
- [22] S. Macfarlane and E.A. Croft. Jerk-bounded manipulator trajectory planning: design for real-time applications. *IEEE Transactions on Robotics and Automation*, 19(1):42–52, February 2003.
- [23] W. Singhose, W. Seering, and N. Singer. Residual vibration reduction using vector diagrams to generate shaped inputs. *Journal of Mechanical Design*, 116(2):654–659, June 1994.
- [24] Joshua Vaughan, Aika Yano, and William Singhose. Comparison of robust input shapers. *Journal of Sound and Vibration*, 315(4-5):797–815, sep 2008.
- [25] W.E. Singhose, W.P. Seering, and N.C. Singer. Shaping inputs to reduce vibration: a vector diagram approach. In *Proceedings., IEEE International Conference on Robotics and Automation*. IEEE Comput. Soc. Press, 1990.
- [26] Gonzalez-Villagomez Esau, Rodriguez-Donate Carlos, Mata-Chavez Ruth Ivonne, Cabal-Yepey Eduardo, Lopez-Hernandez Juan Manuel, and Palillero-Sandoval Omar. Novel gaussian acceleration profile for smooth jerk-bounded trajectories. *IEEE Access*, 10:120714–120723, 2022.
- [27] W.E. Singhose, Neil Singer, Convolv Inc, and Warren Seering. Design and implementation of time-optimal negative input shapers. March 1996.
- [28] Dongwook Lee and Chang-Wan Ha. Optimization process for polynomial motion profiles to achieve fast movement with low vibration. *IEEE Transactions on Control Systems Technology*, 28(5):1892–1901, September 2020.
- [29] Masaki Haneda, Yukako Ikegami, Kengo Kotoo, Kan Shimizu, Yoshihisa Kagawa, and Hayato Iwamoto. Wafer-on-wafer-on-wafer (wowow) integration having large-scale high reliability fine 1 μm pitch face-to-back (f2b) cu-cu connections and fine 6 μm pitch tsvs. In *2024 IEEE 74th Electronic Components and Technology Conference (ECTC)*, pages 1342–1346. IEEE, May 2024.
- [30] Chul-Goo Kang. Impulse vectors for input-shaping control: A mathematical tool to design and analyze input shapers. *IEEE Control Systems*, 39(4):40–55, aug 2019.
- [31] Mateusz Kasprowiak, Arkadiusz Parus, and Marcin Hoffmann. Vibration suppression with use of input shaping control in machining. *Sensors*, 22(6):2186, mar 2022.
- [32] Yukako Ikegami, Takumi Onodera, Masanori Chiyozono, Akihisa Sakamoto, Kan Shimizu, Yoshihisa Kagawa, and Hayato Iwamoto. Study of ultra-fine 0.4 μm pitch wafer-to-wafer hybrid bonding and impact of bonding misalignment. In *2024 IEEE 74th Electronic Components and Technology Conference (ECTC)*, pages 299–304. IEEE, May 2024.
- [33] Cristiana Silva and Emmanuel Trelat. Smooth regularization of bang-bang optimal control problems. *IEEE Transactions on Automatic Control*, 55(11):2488–2499, November 2010.
- [34] Markos Papageorgiou, Marion Leibold, and Martin Buss. *Optimierung - Statische, dynamische, stochastische Verfahren für die Anwendung*. Springer Berlin Heidelberg, Berlin, Heidelberg, 4., neu bearb. u. erg. aufl. 2015 edition, 2015.
- [35] B.G. Dijkstra, N.J. Rambaratsingh, C. Scherer, O.H. Bosgra, M. Steinbuch, and S. Kerssemakers. Input design for optimal discrete time point-to-point motion of an industrial xy-positioning table. In *Proceedings of the 39th IEEE Conference on Decision and Control (Cat. No.00CH37187)*, CDC-00. IEEE, 2007.
- [36] U. H. Park, J. W. Lee, B. D. Lim, and Y. G. Sung. Design and Sensitivity Analysis of an Input Shaping Filter in the Z-Plane. *Journal of Sound and Vibration*, 243(1):157–171, May 2001.
- [37] Jinhua She, Lulu Wu, and Zhen-Tao Liu. Combining input shaping and adaptive model-following control for vibration suppression. *Journal of Advanced Computational Intelligence and Intelligent Informatics*, 25(1):56–63, January 2021.
- [38] C.R. Hargraves and S.W. Paris. Direct trajectory optimization using nonlinear programming and collocation. *Journal of Guidance, Control, and Dynamics*, 10(4):338–342, July 1987.
- [39] Dan Pilbauer, Wim Michiels, Jaroslav Bušek, David Osta, and Tomáš Vyhldal. Control design and experimental validation for flexible multi-body systems pre-compensated by inverse shapers. *Systems & Control Letters*, 113:93–100, March 2018.
- [40] Rajanya Yalamanchili, Stefan Schlee, Markus Märkl, and Frank A. King. Enhanced time-optimal filter-based point-to-point trajectory generation with vibration suppression. In *2024 10th International Conference on Mechatronics and Robotics Engineering (ICMRE)*, pages 10–17. IEEE, February 2024.
- [41] Leslie M. Hocking. *Optimal Control - An Introduction to the Theory with Applications*. Oxford University PressOxford, February 1991.
- [42] Thomas Auer and Frank Woittennek. Calculation of time-optimal motion primitives for systems exhibiting oscillatory internal dynamics. *preprint*, 2025.
- [43] Thomas Auer and Frank Woittennek. On improving the settling time for highly-accurate pick-and-place processes with experimental validation.

- In 2024 *IEEE 20th International Conference on Automation Science and Engineering (CASE)*, pages 3683–3690. IEEE, August 2024.
- [44] John T. Betts. Survey of numerical methods for trajectory optimization. *Journal of Guidance, Control, and Dynamics*, 21(2):193–207, mar 1998.
- [45] Luigi Biagiotti, Claudio Melchiorri, and Lorenzo Moriello. Damped harmonic smoother for trajectory planning and vibration suppression. *IEEE Transactions on Control Systems Technology*, 28(2):626–634, March 2020.
- [46] A. Piazzi and A. Visioli. Global minimum-jerk trajectory planning of robot manipulators. *IEEE Transactions on Industrial Electronics*, 47(1):140–149, 2000.
- [47] Luigi Biagiotti and Claudio Melchiorri. Optimization of generalized s-curve trajectories for residual vibration suppression and compliance with kinematic bounds. *IEEE/ASME Transactions on Mechatronics*, 26(5):2724–2734, October 2021.
- [48] Chengkai Dai, Sylvain Lefebvre, Kai-Ming Yu, Jo M. P. Geraedts, and Charlie C. L. Wang. Planning jerk-optimized trajectory with discrete time constraints for redundant robots. *IEEE Transactions on Automation Science and Engineering*, 17(4):1711–1724, October 2020.
- [49] T. H. Tsang, D. M. Himmelblau, and T. F. Edgar. Optimal control via collocation and non-linear programming. *International Journal of Control*, 21(5):763–768, May 1975.
- [50] John H Lau. Current advances and outlooks in hybrid bonding. *IEEE Transactions on Components, Packaging and Manufacturing Technology*, pages 1–1, 2025.
- [51] Michael Athans and Peter L. Falb. *Optimal control - An Introduction to the Theory and Its Applications*. Dover Publ., Mineola, New York, 2007.
- [52] Lucy Y. Pao and William E. Singhose. Robust minimum time control of flexible structures. *Automatica*, 34(2):229–236, feb 1998.
- [53] Wilson Linda S., Balestra Francis, Sangiorgi Enrico, Hayashi Yoshihiro, Takaura Norikatsu, Ishiuchi Hidemi, Gargini Paolo, and Conte Tom. International Roadmap for Devices and Systems (IRDS). Technical report, IEEE, 2023.
- [54] Robbert van der Kruk, Arend Jan van Noorden, Tom Oomen, René van de Molengraft, and Herman Bruyninckx. Robotic control for vibration reduction of swinging products. In *2023 IEEE International Conference on Mechatronics (ICM)*. IEEE, March 2023.
- [55] Hazrat Bilal, Baoqun Yin, Aakash Kumar, Munawar Ali, Jing Zhang, and Jinfa Yao. Jerk-bounded trajectory planning for rotary flexible joint manipulator: an experimental approach. *Soft Computing*, 27(7):4029–4039, February 2023.

APPENDIX A

ALGORITHMS FOR IMPLEMENTATION

This section contains the calculations necessary to compute a complete OCP-J trajectory without violating any kinematic constraints. As mentioned earlier, a trajectory for a given a_{\max} is computed using Algorithm 1. This calculation is called in

Algorithm 1 Get OCP-J trajectory for a_{\max}

- 1: Get segment for a_{\max} ▷ Use [42]
 - 2: Get segment for $2 a_{\max}$ ▷ Use [42]
 - 3: Calculate s_{f1}, \dots, v_{f3}
 - 4: Calculate OCP-J trajectory for Case 1
 - 5: **if** $v(t) \leq v_{\text{lim}} \forall t \in [0, t_{f,t}]$ **then**
 - 6: **return** OCP-J trajectory for Case 1
 - 7: **else**
 - 8: **if** $s(t_f) \geq s_{f,\text{min-Case 2}}$ **then**
 - 9: Calculate OCP-J trajectory for Case 2
 - 10: **return** OCP-J trajectory for Case 2
 - 11: **else**
 - 12: Calculate OCP-J trajectory for Case 3
 - 13: **return** OCP-J trajectory for Case 3
 - 14: **end if**
 - 15: **end if**
-

Algorithm 2 and the kinematic constraints are checked. If

Algorithm 2 Get OCP-J total

- 1: Calculate a_{best} with (23) ▷ Only required once
 - 2: Limit a_{best} to a_{lim}
 - 3: Calculate OCP-J trajectory with Algorithm 1 for a_{best}
 - 4: **if** $a(t) \leq a_{\text{lim}}$ and $j(t) \leq j_{\text{lim}} \forall t \in [0, t_{f,t}]$ **then**
 - 5: **return** OCP-J trajectory
 - 6: **else**
 - 7: Run Algorithm 3
 - 8: **return** OCP-J trajectory
 - 9: **end if**
-

the kinematic constraints are not violated, the computation is finished and the computed trajectory can be exported, otherwise Algorithm 3 must be called. A search algorithm iterates over possible a_{\max} values and searches for the highest possible a_{\max} where no kinematic constraint is violated. This can be achieved efficiently with a binary search as described in Algorithm 3. The bounds for the terminal conditions $\Delta t_{\text{boundary}}$ and $n_{\text{max-iter}}$ can be set as follows. The time $\Delta t_{\text{boundary}}$ can be set to one controller cycle interval from the system. If the improvement in time Δt_f is less than one controller cycle, the calculation can be stopped. When implementing the algorithm in single precision (the measurements in Subsection VI-C show, that this can already be sufficient), the upper limit for $n_{\text{max-iter}}$ can be set to $n_{\text{max-iter}} = 23$. Iterating more than the number of significant digits of the single precision variable does not provide any benefit. Setting these limits for $n_{\text{max-iter}}$ and $\Delta t_{\text{boundary}}$ ensures that the search algorithm will stop after a given number of iterations.

Algorithm 3 Optimize a_{\max}

- 1: Initialize $\Delta a_{\text{ges}} = a_{\text{best}}$
 - 2: Set $n_{\text{iter}} = 1$
 - 3: Set $a_{\text{iter}} = \frac{1}{2} \Delta a_{\text{ges}}$
 - 4: **repeat**
 - 5: Get trajectory with Algorithm 1 for $a_{\max} = a_{\text{iter}}$
 - 6: $n_{\text{iter}} = n_{\text{iter}} + 1$
 - 7: **if** $a(t) \leq a_{\text{lim}}$ and $j(t) \leq j_{\text{lim}} \forall t \in [0, t_{f,t}]$ **then**
 - 8: Save $t_{f,t}$ and calculate $\Delta t_f = t_{f,t;(k-1)} - t_{f,t;k}$
 - 9: **if** $t_{f,t;k} < t_{f,\text{best}}$ **then**
 - 10: $t_{f,\text{best}} = t_{f,t;k}$
 - 11: Save trajectory for export
 - 12: **end if**
 - 13: Set $a_{\text{iter}} = a_{\text{iter}} + \left(\frac{1}{2}\right)^{n_{\text{iter}}} \cdot \Delta a_{\text{ges}}$
 - 14: **else**
 - 15: Set $a_{\text{iter}} = a_{\text{iter}} - \left(\frac{1}{2}\right)^{n_{\text{iter}}} \cdot \Delta a_{\text{ges}}$
 - 16: **end if**
 - 17: **until** $\Delta t_f \leq \Delta t_{\text{boundary}} \vee n_{\text{iter}} > n_{\text{max-iter}}$
 - 18: **return** Trajectory from step 11 of Alg.
-

APPENDIX B
MEASUREMENT RESULTS

TABLE VI: Measurement results: Listing amplitudes at $t_{f,t}$ for measured distances, trajectory planning methods and parameter combinations according to Table IV.

$z(t_f) = 14.5 \text{ mm}$						
Method	$t_{f,t}$	$f_{\text{sys}} = 8.71 \text{ Hz}$	$f_{\text{sys}} = 9.20 \text{ Hz}$	$f_{\text{sys}} = f_{\text{nom}} = 9.71 \text{ Hz}$	$f_{\text{sys}} = 10.27 \text{ Hz}$	$f_{\text{sys}} = 10.60 \text{ Hz}$
S-Curve	132.8 ms	$a_{\text{max}} = 853.67 \mu\text{m}$ $a_{\text{min}} = 846.98 \mu\text{m}$	$a_{\text{max}} = 751.30 \mu\text{m}$ $a_{\text{min}} = 746.07 \mu\text{m}$	$a_{\text{max}} = 645.37 \mu\text{m}$ $a_{\text{min}} = 643.77 \mu\text{m}$	$a_{\text{max}} = 533.54 \mu\text{m}$ $a_{\text{min}} = 527.82 \mu\text{m}$	$a_{\text{max}} = 487.78 \mu\text{m}$ $a_{\text{min}} = 482.18 \mu\text{m}$
ZV	184.4 ms	$a_{\text{max}} = 130.35 \mu\text{m}$ $a_{\text{min}} = 128.99 \mu\text{m}$	$a_{\text{max}} = 51.83 \mu\text{m}$ $a_{\text{min}} = 50.40 \mu\text{m}$	$a_{\text{max}} = 12.09 \mu\text{m}$ $a_{\text{min}} = 11.28 \mu\text{m}$	$a_{\text{max}} = 60.03 \mu\text{m}$ $a_{\text{min}} = 58.99 \mu\text{m}$	$a_{\text{max}} = 75.05 \mu\text{m}$ $a_{\text{min}} = 73.74 \mu\text{m}$
FIR _{Imp}	156.4 ms	$a_{\text{max}} = 200.82 \mu\text{m}$ $a_{\text{min}} = 199.66 \mu\text{m}$	$a_{\text{max}} = 94.83 \mu\text{m}$ $a_{\text{min}} = 93.23 \mu\text{m}$	$a_{\text{max}} = 22.17 \mu\text{m}$ $a_{\text{min}} = 19.63 \mu\text{m}$	$a_{\text{max}} = 99.30 \mu\text{m}$ $a_{\text{min}} = 98.21 \mu\text{m}$	$a_{\text{max}} = 131.88 \mu\text{m}$ $a_{\text{min}} = 130.17 \mu\text{m}$
OCP-J	162.4 ms	$a_{\text{max}} = 171.35 \mu\text{m}$ $a_{\text{min}} = 168.55 \mu\text{m}$	$a_{\text{max}} = 75.03 \mu\text{m}$ $a_{\text{min}} = 73.64 \mu\text{m}$	$a_{\text{max}} = 8.35 \mu\text{m}$ $a_{\text{min}} = 7.94 \mu\text{m}$	$a_{\text{max}} = 80.40 \mu\text{m}$ $a_{\text{min}} = 79.46 \mu\text{m}$	$a_{\text{max}} = 106.50 \mu\text{m}$ $a_{\text{min}} = 104.49 \mu\text{m}$
$z(t_f) = 61 \text{ mm}$						
Method	$t_{f,t}$	$f_{\text{sys}} = 8.71 \text{ Hz}$	$f_{\text{sys}} = 9.20 \text{ Hz}$	$f_{\text{sys}} = f_{\text{nom}} = 9.71 \text{ Hz}$	$f_{\text{sys}} = 10.27 \text{ Hz}$	$f_{\text{sys}} = 10.60 \text{ Hz}$
S-Curve	240.8 ms	$a_{\text{max}} = 464.30 \mu\text{m}$ $a_{\text{min}} = 459.90 \mu\text{m}$	$a_{\text{max}} = 500.02 \mu\text{m}$ $a_{\text{min}} = 496.75 \mu\text{m}$	$a_{\text{max}} = 479.34 \mu\text{m}$ $a_{\text{min}} = 478.30 \mu\text{m}$	$a_{\text{max}} = 404.07 \mu\text{m}$ $a_{\text{min}} = 402.72 \mu\text{m}$	$a_{\text{max}} = 363.29 \mu\text{m}$ $a_{\text{min}} = 357.85 \mu\text{m}$
ZV	292.4 ms	$a_{\text{max}} = 71.14 \mu\text{m}$ $a_{\text{min}} = 69.80 \mu\text{m}$	$a_{\text{max}} = 35.21 \mu\text{m}$ $a_{\text{min}} = 33.57 \mu\text{m}$	$a_{\text{max}} = 4.74 \mu\text{m}$ $a_{\text{min}} = 3.86 \mu\text{m}$	$a_{\text{max}} = 42.40 \mu\text{m}$ $a_{\text{min}} = 41.12 \mu\text{m}$	$a_{\text{max}} = 51.98 \mu\text{m}$ $a_{\text{min}} = 50.89 \mu\text{m}$
FIR _{Imp}	260.4 ms	$a_{\text{max}} = 132.01 \mu\text{m}$ $a_{\text{min}} = 130.73 \mu\text{m}$	$a_{\text{max}} = 80.20 \mu\text{m}$ $a_{\text{min}} = 78.90 \mu\text{m}$	$a_{\text{max}} = 20.13 \mu\text{m}$ $a_{\text{min}} = 18.63 \mu\text{m}$	$a_{\text{max}} = 100.01 \mu\text{m}$ $a_{\text{min}} = 99.57 \mu\text{m}$	$a_{\text{max}} = 133.39 \mu\text{m}$ $a_{\text{min}} = 132.33 \mu\text{m}$
OCP-J	273.6 ms	$a_{\text{max}} = 87.32 \mu\text{m}$ $a_{\text{min}} = 85.28 \mu\text{m}$	$a_{\text{max}} = 44.09 \mu\text{m}$ $a_{\text{min}} = 43.72 \mu\text{m}$	$a_{\text{max}} = 5.24 \mu\text{m}$ $a_{\text{min}} = 3.34 \mu\text{m}$	$a_{\text{max}} = 51.34 \mu\text{m}$ $a_{\text{min}} = 50.49 \mu\text{m}$	$a_{\text{max}} = 64.60 \mu\text{m}$ $a_{\text{min}} = 64.22 \mu\text{m}$
$z(t_f) = 116 \text{ mm}$						
Method	$t_{f,t}$	$f_{\text{sys}} = 8.71 \text{ Hz}$	$f_{\text{sys}} = 9.20 \text{ Hz}$	$f_{\text{sys}} = f_{\text{nom}} = 9.71 \text{ Hz}$	$f_{\text{sys}} = 10.27 \text{ Hz}$	$f_{\text{sys}} = 10.60 \text{ Hz}$
S-Curve	362.8 ms	$a_{\text{max}} = 574.02 \mu\text{m}$ $a_{\text{min}} = 567.43 \mu\text{m}$	$a_{\text{max}} = 633.81 \mu\text{m}$ $a_{\text{min}} = 629.54 \mu\text{m}$	$a_{\text{max}} = 554.17 \mu\text{m}$ $a_{\text{min}} = 552.22 \mu\text{m}$	$a_{\text{max}} = 356.40 \mu\text{m}$ $a_{\text{min}} = 353.13 \mu\text{m}$	$a_{\text{max}} = 262.14 \mu\text{m}$ $a_{\text{min}} = 257.48 \mu\text{m}$
ZV	414.4 ms	$a_{\text{max}} = 86.33 \mu\text{m}$ $a_{\text{min}} = 86.12 \mu\text{m}$	$a_{\text{max}} = 41.83 \mu\text{m}$ $a_{\text{min}} = 40.83 \mu\text{m}$	$a_{\text{max}} = 6.85 \mu\text{m}$ $a_{\text{min}} = 5.51 \mu\text{m}$	$a_{\text{max}} = 37.07 \mu\text{m}$ $a_{\text{min}} = 35.10 \mu\text{m}$	$a_{\text{max}} = 36.17 \mu\text{m}$ $a_{\text{min}} = 35.48 \mu\text{m}$
FIR _{Imp}	382.8 ms	$a_{\text{max}} = 159.30 \mu\text{m}$ $a_{\text{min}} = 157.40 \mu\text{m}$	$a_{\text{max}} = 94.53 \mu\text{m}$ $a_{\text{min}} = 92.42 \mu\text{m}$	$a_{\text{max}} = 25.64 \mu\text{m}$ $a_{\text{min}} = 24.15 \mu\text{m}$	$a_{\text{max}} = 87.92 \mu\text{m}$ $a_{\text{min}} = 86.49 \mu\text{m}$	$a_{\text{max}} = 97.86 \mu\text{m}$ $a_{\text{min}} = 96.66 \mu\text{m}$
OCP-J	395.2 ms	$a_{\text{max}} = 101.24 \mu\text{m}$ $a_{\text{min}} = 99.84 \mu\text{m}$	$a_{\text{max}} = 49.87 \mu\text{m}$ $a_{\text{min}} = 49.16 \mu\text{m}$	$a_{\text{max}} = 3.56 \mu\text{m}$ $a_{\text{min}} = 2.93 \mu\text{m}$	$a_{\text{max}} = 42.07 \mu\text{m}$ $a_{\text{min}} = 41.25 \mu\text{m}$	$a_{\text{max}} = 43.42 \mu\text{m}$ $a_{\text{min}} = 41.93 \mu\text{m}$
$z(t_f) = 139 \text{ mm}$						
Method	$t_{f,t}$	$f_{\text{sys}} = 8.71 \text{ Hz}$	$f_{\text{sys}} = 9.20 \text{ Hz}$	$f_{\text{sys}} = f_{\text{nom}} = 9.71 \text{ Hz}$	$f_{\text{sys}} = 10.27 \text{ Hz}$	$f_{\text{sys}} = 10.60 \text{ Hz}$
S-Curve	414 ms	$a_{\text{max}} = 724.58 \mu\text{m}$ $a_{\text{min}} = 715.57 \mu\text{m}$	$a_{\text{max}} = 354.98 \mu\text{m}$ $a_{\text{min}} = 353.54 \mu\text{m}$	$a_{\text{max}} = 74.41 \mu\text{m}$ $a_{\text{min}} = 72.00 \mu\text{m}$	$a_{\text{max}} = 222.30 \mu\text{m}$ $a_{\text{min}} = 220.94 \mu\text{m}$	$a_{\text{max}} = 258.53 \mu\text{m}$ $a_{\text{min}} = 253.75 \mu\text{m}$
ZV	465.6 ms	$a_{\text{max}} = 92.36 \mu\text{m}$ $a_{\text{min}} = 89.93 \mu\text{m}$	$a_{\text{max}} = 21.79 \mu\text{m}$ $a_{\text{min}} = 20.34 \mu\text{m}$	$a_{\text{max}} = 5.25 \mu\text{m}$ $a_{\text{min}} = 4.82 \mu\text{m}$	$a_{\text{max}} = 24.68 \mu\text{m}$ $a_{\text{min}} = 23.12 \mu\text{m}$	$a_{\text{max}} = 35.99 \mu\text{m}$ $a_{\text{min}} = 34.95 \mu\text{m}$
FIR _{Imp}	414 ms	$a_{\text{max}} = 723.64 \mu\text{m}$ $a_{\text{min}} = 718.85 \mu\text{m}$	$a_{\text{max}} = 353.73 \mu\text{m}$ $a_{\text{min}} = 351.89 \mu\text{m}$	$a_{\text{max}} = 74.41 \mu\text{m}$ $a_{\text{min}} = 73.36 \mu\text{m}$	$a_{\text{max}} = 222.23 \mu\text{m}$ $a_{\text{min}} = 221.46 \mu\text{m}$	$a_{\text{max}} = 257.77 \mu\text{m}$ $a_{\text{min}} = 252.73 \mu\text{m}$
OCP-J	446.4 ms	$a_{\text{max}} = 109.91 \mu\text{m}$ $a_{\text{min}} = 106.53 \mu\text{m}$	$a_{\text{max}} = 24.51 \mu\text{m}$ $a_{\text{min}} = 22.91 \mu\text{m}$	$a_{\text{max}} = 5.01 \mu\text{m}$ $a_{\text{min}} = 3.45 \mu\text{m}$	$a_{\text{max}} = 28.14 \mu\text{m}$ $a_{\text{min}} = 26.98 \mu\text{m}$	$a_{\text{max}} = 42.80 \mu\text{m}$ $a_{\text{min}} = 41.74 \mu\text{m}$
$z(t_f) = 181 \text{ mm}$						
Method	$t_{f,t}$	$f_{\text{sys}} = 8.71 \text{ Hz}$	$f_{\text{sys}} = 9.20 \text{ Hz}$	$f_{\text{sys}} = f_{\text{nom}} = 9.71 \text{ Hz}$	$f_{\text{sys}} = 10.27 \text{ Hz}$	$f_{\text{sys}} = 10.60 \text{ Hz}$
S-Curve	507.6 ms	$a_{\text{max}} = 817.42 \mu\text{m}$ $a_{\text{min}} = 806.26 \mu\text{m}$	$a_{\text{max}} = 554.20 \mu\text{m}$ $a_{\text{min}} = 551.92 \mu\text{m}$	$a_{\text{max}} = 186.82 \mu\text{m}$ $a_{\text{min}} = 183.39 \mu\text{m}$	$a_{\text{max}} = 184.74 \mu\text{m}$ $a_{\text{min}} = 183.51 \mu\text{m}$	$a_{\text{max}} = 241.01 \mu\text{m}$ $a_{\text{min}} = 238.01 \mu\text{m}$
ZV	558.8 ms	$a_{\text{max}} = 103.51 \mu\text{m}$ $a_{\text{min}} = 102.12 \mu\text{m}$	$a_{\text{max}} = 28.53 \mu\text{m}$ $a_{\text{min}} = 26.37 \mu\text{m}$	$a_{\text{max}} = 4.87 \mu\text{m}$ $a_{\text{min}} = 3.48 \mu\text{m}$	$a_{\text{max}} = 21.84 \mu\text{m}$ $a_{\text{min}} = 21.37 \mu\text{m}$	$a_{\text{max}} = 33.83 \mu\text{m}$ $a_{\text{min}} = 33.19 \mu\text{m}$
FIR _{Imp}	515.2 ms	$a_{\text{max}} = 818.45 \mu\text{m}$ $a_{\text{min}} = 817.10 \mu\text{m}$	$a_{\text{max}} = 453.56 \mu\text{m}$ $a_{\text{min}} = 450.09 \mu\text{m}$	$a_{\text{max}} = 101.22 \mu\text{m}$ $a_{\text{min}} = 98.77 \mu\text{m}$	$a_{\text{max}} = 289.66 \mu\text{m}$ $a_{\text{min}} = 286.55 \mu\text{m}$	$a_{\text{max}} = 318.30 \mu\text{m}$ $a_{\text{min}} = 313.76 \mu\text{m}$
OCP-J	539.6 ms	$a_{\text{max}} = 120.42 \mu\text{m}$ $a_{\text{min}} = 118.61 \mu\text{m}$	$a_{\text{max}} = 32.65 \mu\text{m}$ $a_{\text{min}} = 30.77 \mu\text{m}$	$a_{\text{max}} = 3.56 \mu\text{m}$ $a_{\text{min}} = 2.75 \mu\text{m}$	$a_{\text{max}} = 26.40 \mu\text{m}$ $a_{\text{min}} = 25.65 \mu\text{m}$	$a_{\text{max}} = 40.41 \mu\text{m}$ $a_{\text{min}} = 39.22 \mu\text{m}$